MASTER

Measurements of shock waves using Thomson- and Rayleigh scattering on an expanding cascaded arc plasma

Janssen, G.M.

Award date:
2001

Eindhoven University of Technology
Department of physics
"Vakgroep Deeltjesfysica"
"Onderwerpgroep E.T.P."

Measurements of shock waves using Thomson– and Rayleigh scattering on an expanding cascaded arc plasma

Ger Janssen
june 1991

Supervisor: Richard van de Sanden

Graduation professor: prof. Dr. Ir. D.C. Schram

Summary

Thomson–Rayleigh scattering is a method to measure the electron density n_e, electron temperature T_e and the neutral density n_0 locally in a plasma. This makes it possible to study shock wave phenomena in expanding plasmas. The measurements are performed on an argon plasma which expands from a cascaded arc into a vessel at low pressure.
A method is developed, using least mean square analysis, to calculate the three plasma parameters accurate. The reached accuracy in n_e is $1-4$ %, for T_e $2-4$ % and for n_0 10 $-$ 20 %, depending on the conditions.
A standing shock wave occurs in the electron and neutral density. The position of the jump in T_e occurs closer to the expansion than the jumps in n_e and n_0. This is probably caused by current generation due to the strong pressure gradient in the first part of the expansion. The current generation is calculated with the electron energy balance.

Contents

1 Introduction

To understand the physical phenomena in expanding plasmas, knowledge of the most important plasma parameters as densities and temperatures is essential. Combined Thomson–Rayleigh scattering gives a means to measure three plasma parameters locally, namely the electron density, electron temperature and the neutral density.
The aims of this work are:

- To develop a method and a Turbo Pascal program to fit Thomson–Rayleigh scattering measurements. From the fits the plasma parameters can then be calculated;
- Investigation on shock wave phenomena occurring in expanding plasmas.

A Thomson–Rayleigh scattering measurement consists of a Thomson component and a Rayleigh component. The Thomson component accounts for the scattering on free electrons, while the Rayleigh component reflects the scattering on bounded electrons of neutral atoms and ions. In earlier days the plasma parameters were calculated with a Thomson plot or directly from the scattered spectrum [1], [2]. A fit program is developed to reach a higher accuracy in the determination of the plasma parameters [2], [3]. Also deviations from a Maxwellian velocity distribution function for the electrons can easily be studied. Connected with the fit program corrections for collective effects are introduced, i.e. when the scattered spectrum depends on the collective behavior of groups of electrons.

Most measurements done in this work show a shock structure in the plasma parameters. Remarkable is that the jump in the electron temperature occurs earlier than the jump in the electron and neutral densities. For normal shocks the position of the jumps is the same [4]. Investigations on shock tubes show contradictory results. For example, in ref. [5] the position of the jump in the electron temperature and the jump in the densities is the same, while ref. [6] clearly shows a difference between the positions of the jumps. We explain this difference by means of current generation due to the strong pressure gradient in the first part of the expansion. The electron temperature then increases by means of Ohmic heating. The current density can be calculated with the electron energy balance.

In chapter 2 the theory of scattering of electromagnetic radiation by a plasma is treated. Beside scattering on individual electrons, the incoherent scattering, corrections for collective effects are introduced. Chapter 3 discusses the cascaded arc set up and the Thomson–Rayleigh scattering set up, present at the Plasma Physics Group of the Physics Department of the Eindhoven University of Technology. Also the necessary calibrations are considered.

The developed fitting method for the combined Thomson–Rayleigh scattering measurements is treated, tested and discussed in chapter 4. In chapter 5 the theory of shock waves is treated shortly as introduction for chapter 6.

Chapter 6 deals with the results of the scattering measurements. In particular the shock structure of the expanding cascaded arc plasma is discussed.

The current density on the axis of an expanding plasma is calculated using the electron energy balance. The energy balance and results are discussed in chapter 7. Finally in chapter 8 the conclusions and some suggestions are given.

2 Scattering of electromagnetic radiation by a plasma

2.1 Introduction

When electromagnetic radiation strikes a charged particle, the oscillating electromagnetic field of the radiation accelerates the particle in resonance with the incident field. The accelerated charged particle will now act as a radiating dipole oscillator and emits radiation [7]. See figure 2.1.

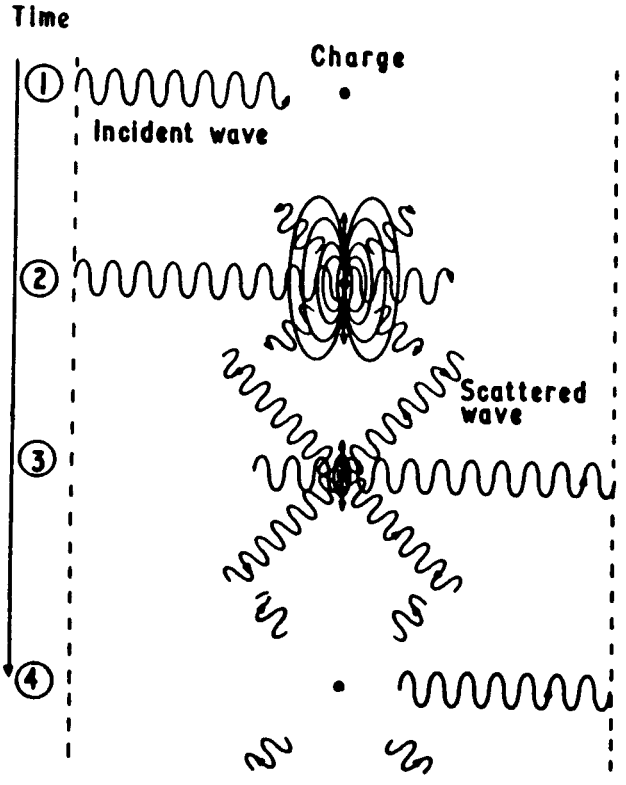

Figure 2.1 Scattering of radiation by a free charged particle.

The spectrum of the scattered radiation depends on the electron density n_e, electron and ion temperatures T_e and T_i respectively, and also the neutral density n_0. In this chapter we derive expressions to calculate n_e, T_e and n_0 from the scattered spectrum.

2.2 Scattering on a moving particle

We consider a charged particle moving with a velocity **v**. The incident electromagnetic radiation with wave vector $\mathbf{k}_i$ ($|\mathbf{k}_i| = 2\pi/\lambda_i$) is scattered by the charged particle. The wave vector of the scattered radiation is $\mathbf{k}_s$. See figure 2.2. Because the particle is moving the scattered radiation will be Doppler–shifted.

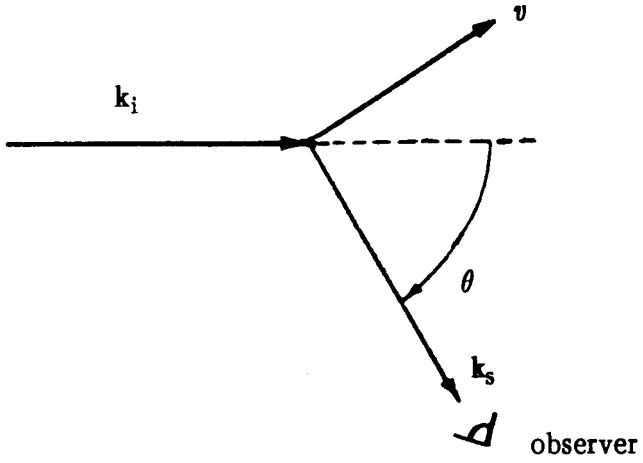

Figure 2.2 Scattering geometry for scattering on a moving particle.

The scattered radiation is angle dependent. This dependency is shown in figure 2.3. The radiation field is just that of a radiating dipole.

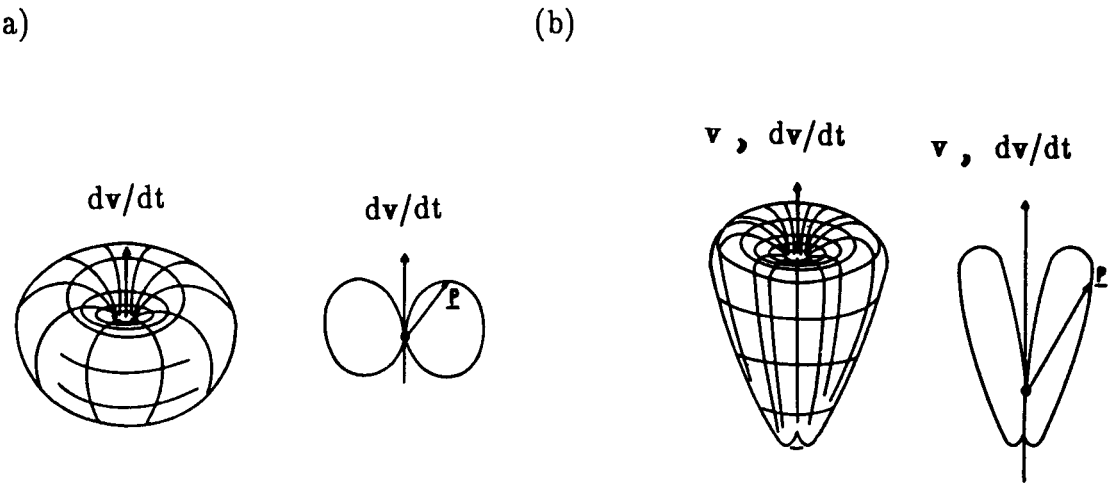

Figure 2.3 The angular variation of the radiation scattered by an accelerated charge. (a) stationary charge; (b) charge moving with $\mathbf{v} \,//\, d\mathbf{v}/dt$.

At low velocities of the particles ($v \ll c$) the variation of the scattered radiation with direction has the shape shown in figure 2.3a. At higher velocities ($v \leq c$) the radiation is scattered more in the direction of $\mathbf{v}$ [7]. This is shown in figure 2.3b. We assume that no relativistic effects are present, which means $v \ll c$. By choosing an appropriate wavelength of the incoming electromagnetic radiation in our experiment ($\lambda_i = 532$ nm) no quantum effects occur. Then the following relation is valid:

$$|\mathbf{k}_s| \simeq |\mathbf{k}_i| \tag{2.1}$$

We now define a scattering vector $\mathbf{k}$, the shift in wave vector, as

$$\mathbf{k} = \mathbf{k}_s - \mathbf{k}_i \tag{2.2}$$

See figure 2.4.

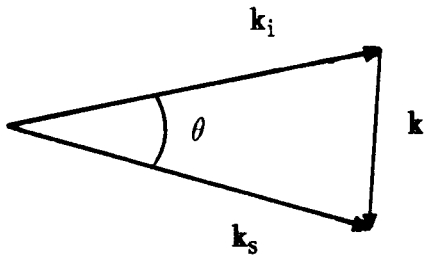

Figure 2.4 Definition of the scattering vector $\mathbf{k}$.

From figure 2.4 we see that:

$$|\mathbf{k}| = (k_s^2 + k_i^2 - 2k_s k_i \cos\theta)^{1/2} \tag{2.3}$$

This leads, together with equation 2.1 to

$$|\mathbf{k}| = 2k_i \sin(\theta/2) \tag{2.4}$$

The Doppler shift of the frequency of the scattered radiation is a result of two effects:

- The incident wave is "seen" by the charged particle at a Doppler–shifted frequency, because the particle is moving with respect to the source of radiation.
- The particle has a velocity component in the direction of the observer which gives a second Doppler shift.

With the definition of the shift in frequency, ω, we have

$$\omega = \omega_s - \omega_i = (\mathbf{k}_s - \mathbf{k}_i)\cdot\mathbf{v} = \mathbf{k}\cdot\mathbf{v} \tag{2.5}$$

So the shift in frequency ω is proportional to the component of the particle velocity in the direction of **k**.
When the scattering particle is a free electron we speak of *Thomson scattering.*

2.3 Incoherent and coherent spectra

In the last paragraph we discussed the scattering on one charged particle. Now we look at the situation in a plasma, which consists of more charged particles. Therefore we introduce a scattering parameter α

$$\alpha = \frac{1}{k\lambda_D} \tag{2.6}$$

with k from equation 2.4 and λ_D the Debye length

$$\lambda_D = \sqrt{\frac{\epsilon_0 k_b T_e}{e^2 n_e}} \tag{2.7}$$

We now consider two cases:

- If $\frac{\lambda_i}{4\pi \sin(\theta/2)} \ll \lambda_D$, which means $\alpha \ll 1$, we have *incoherent scattering.* The incident wave "sees" the individual electrons, which appear free. In this case the scattered spectrum reflects the shape of the electron velocity distribution (this is reasonable from equation 2.5, which shows that ω is proportional to the electron velocity component which lies along **k**).

– If $\frac{\lambda_i}{4\pi \sin(\theta/2)} \geq \lambda_D$, which means $\alpha \geq 1$, we have *coherent scattering.* The incident wave now interacts with shielded charges. The scattered spectrum therefore depends on the collective behavior of groups of charges.

In our Thomson scattering experiments we have a situation in between, i.e. $\alpha < 1$ but **not** $\alpha \ll 1$. This case is more complicated then the case of incoherent scattering. The shape of the scattered spectrum now depends on the scattering parameter α.

2.4 The scattered power spectrum

A general expression for the scattered power in a solid angle $\Delta\Omega$ and in a frequency range $d\omega_s$ (= $d\omega$, equation 2.5) is given by [7]

$$P_s d\omega_s = P_i \cdot n_e \cdot L \cdot \Delta\Omega \cdot g(\theta,\phi_o) \cdot S(\mathbf{k},\omega) \cdot d\sigma_t/d\Omega \cdot d\omega_s \qquad (2.8)$$

See figure 2.5. In our scattering experiments $P_s/P_i \approx 10^{-14}$ (see paragraph 2.6). P_s and P_i are the scattered and incident power respectively, L is the length of the scattering volume ($V = L \cdot A$) in the direction of $\mathbf{k}_i$, $d\sigma_t/d\Omega$ is the differential cross section for Thomson scattering and $S(\mathbf{k},\omega)$ the spectral density function for a low temperature stable plasma. $g(\theta,\phi_o)$ takes into account the polarization of the incident radiation and reflects the dependence on the angles θ and ϕ_o (see figure 2.5):

$$g(\theta,\phi_o) = 1 - \sin^2\theta\cos^2\phi_o \qquad (2.9)$$

with θ and ϕ_o as defined in figure 2.5. In our case $\theta = \phi_o = 90^0$ and thus $g(\theta,\phi_o) = 1$.

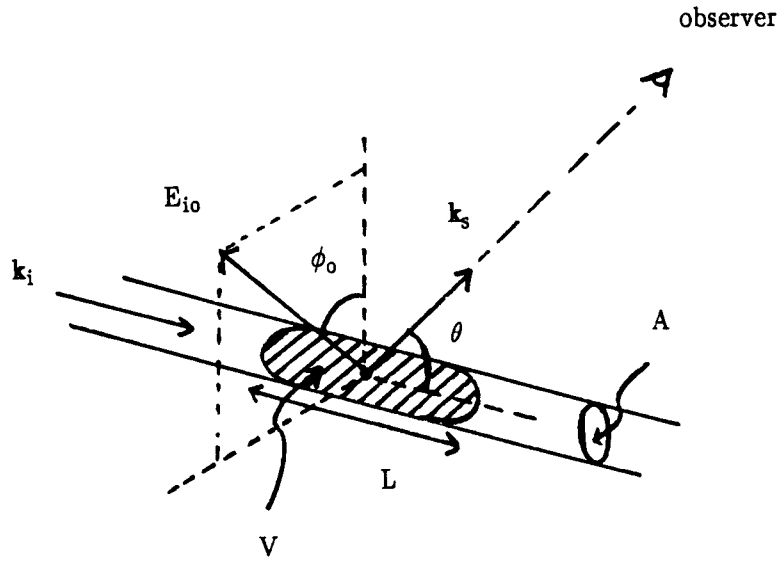

Figure 2.5 The scattering geometry in a plasma.

We now develop an expression for the spectral density function in the case of Maxwellian velocity distribution functions for the electrons and ions. The one–dimensional Maxwellian distribution function is given by:

$$f(v_x) = \frac{1}{(\pi v_{th,x}^2)^{1/2}} \cdot \exp(-v_x^2/v_{th,x}^2) \tag{2.10}$$

with $v_{th,x}$ the thermal speed in the scattering plane of the electrons or ions.

$$v_{th,x} = (2k_b T_x/m_x)^{1/2} \tag{2.11}$$

with x = electrons or ions.
The spectral density function is now in the Salpeter approximation (i.e. it is possible to separate out the properties of the electron and ion features) [7]

$$S(\mathbf{k},\omega) = \frac{1}{k\pi^{1/2} v_{th,e}} \cdot \left[\frac{A_e}{|\epsilon|^2} + \frac{A_i}{|\epsilon|^2} \right] \tag{2.12}$$

where

$$A_e = \exp(-x_e^2)\cdot\left[(1 + \alpha^2 Z\frac{T_e}{T_i}\cdot Rw(x_i))^2 + (\alpha^2 Z\frac{T_e}{T_i}\cdot Iw(x_i))^2\right]$$

$$A_i = Z\cdot\left[\frac{m_i T_e}{m_e T_i}\right]^{1/2}\cdot\exp(-x_i^2)\cdot[(\alpha^2\cdot Rw(x_e))^2 + (\alpha^2\cdot Iw(x_e))^2]$$

$$|\epsilon|^2 = \left[1 + \alpha^2\left[Rw(x_e) + Z\frac{T_e}{T_i}\cdot Rw(x_i)\right]\right]^2 + \left[\alpha^2\cdot Iw(x_e) + \alpha^2 Z\frac{T_e}{T_i}\cdot Iw(x_i)\right]^2 \qquad (2.13)$$

with $x_e = \frac{\omega}{kv_{th,e}}$, $x_i = \frac{\omega}{kv_{th,i}}$, the scattering parameter α from equation 2.6, Z the atomic number and $v_{th,e}$ and $v_{th,i}$ from equation 2.11. In the above equations the following assumptions are made:

- $n_e\lambda_D^3 \gg 1$, where n_e is the electron density and λ_D the Debye length;
- time variations are slow compared to the microscopic times ω_{pe}^{-1}, υ^{-1} and ω_i^{-1} where ω_{pe} is the electron plasma frequency, υ is the collision frequency for momentum transfer and ω_i is the frequency of the incident radiation.

Rw(x) and Iw(x) are the real and imaginary parts of the plasma dispersion function:

$$Rw(x) = 1 - 2x\cdot\exp(-x^2)\cdot\int_0^x \exp(p^2)dp \qquad (2.14)$$

$$Iw(x) = \pi^{1/2}\cdot x\cdot\exp(-x^2) \qquad (2.15)$$

In figure 2.6 the real and imaginary parts of the plasma dispersion function are shown.

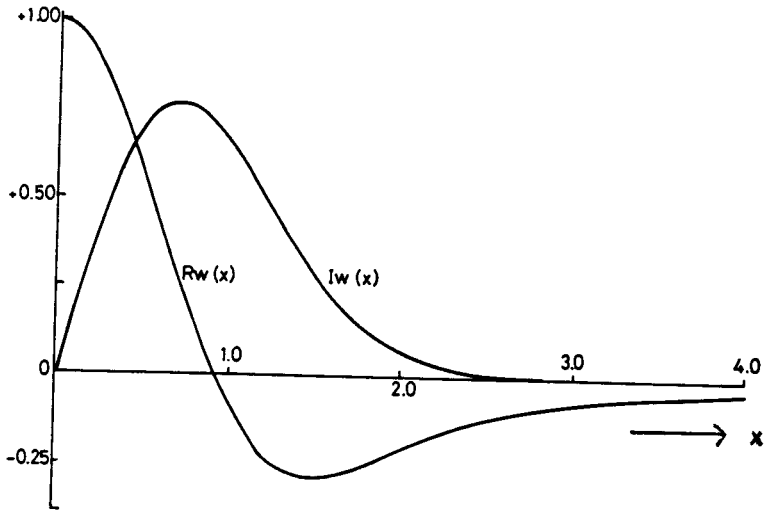

Figure 2.6 The real and imaginary parts of the plasma dispersion function.

For an incoherent spectrum ($\alpha \ll 1$) we get

$$S(\mathbf{k},\omega)\Big|_{\alpha \to 0} = \frac{f_e(\omega/k)}{k} \tag{2.16}$$

with $f_e(\omega/k)$ the one–dimensional Maxwellian distribution function of the electrons (equation 2.10). So

$$\int_{-\infty}^{\infty} S(\mathbf{k},\omega)d\omega_s = \int_{-\infty}^{\infty} f_e(\omega/k)d(\omega/k) = 1 \tag{2.17}$$

with $d\omega_s = d\omega$.

In our Thomson scattering experiments α is not much smaller than one, but $\alpha \leq 0.3$. In this case we can neglect in equation 2.12 the terms proportional with α^4, because the error introduced by this simplification is smaller than 1 %. The equations 2.13 can now be simplified to

$$A_e \simeq \exp(-x_e^2)\cdot\left[1 + \alpha^2 Z\frac{T_e}{T_i}\cdot Rw(x_i)\right]^2$$

$$A_i \simeq 0 \qquad (2.18)$$

$$|\epsilon|^2 \simeq \left[1 + \alpha^2 Z\frac{T_e}{T_i}\cdot Rw(x_i) + \alpha^2\cdot Rw(x_e)\right]^2$$

Substitution of equations 2.18 in equation 2.12 gives

$$S(\mathbf{k},\omega) = \frac{1}{k\pi^{1/2}v_{th,e}}\cdot\exp(-x_e^2)\cdot\frac{[1 + \alpha^2 Z\frac{T_e}{T_i}\cdot Rw(x_i)]^2}{[1 + \alpha^2 Z\frac{T_e}{T_i}\cdot Rw(x_i) + \alpha^2 Rw(x_e)]^2} \qquad (2.19)$$

By further simplification of the right hand side of the above equation (by expanding the denominator as a series expansion and neglecting the α^4 terms) we get

$$S(\mathbf{k},\omega) = \frac{1}{k\pi^{1/2}v_{th,e}}\cdot\exp(-x_e^2)\cdot[1 - 2\alpha^2\cdot Rw(x_e)] \qquad (2.20)$$

$$= \frac{f_e(\omega/k)}{k}\cdot[1 - 2\alpha^2\cdot Rw(x_e)]$$

Integration over ω_s gives

$$\int_{-\infty}^{\infty} S(\mathbf{k},\omega)d\omega_s = 1 - \alpha^2 \qquad (2.21)$$

This looks as if we lose photons. However $S(\mathbf{k},\omega)$ should also be integrated over $\mathbf{k}$. Then the result of the integral would be 1.

We now discuss the consequences of the two solutions equation 2.16 and equation 2.20 for the calculation of the electron density n_e and electron temperature T_e.

a. Incoherent scattering ($\alpha \ll 1$).

From the integration of the scattered power (equation 2.8) over ω_s, it can be shown for incoherent scattering, with substitution of equation 2.17, that the scattered spectrum is pure Gaussian. We then see that n_e is proportional to the area under the Gaussian profile (the total amount of Thomson photons). See also figure 2.7a.
The electron temperature T_e is calculated from the one–over–e width of the Gaussian: the width of the Gaussian where the signal is lowered to 1/e times the maximum signal. We get from equation 2.10

$$\tfrac{1}{2}m_e v_e^2 = k_b T_e \tag{2.22}$$

We also know $\omega_i/c = k_i = 2\pi/\lambda_i$, so differentiating gives

$$|d\omega_i| = \omega = 2\pi c \cdot \frac{d\lambda}{\lambda_i^2} \tag{2.23}$$

Substitution of equation 2.4 and 2.5 in equation 2.23 then gives an expression for the velocity of the electrons, with $d\lambda \equiv \Delta\lambda_{1/e}$ (the half one–over–e width):

$$v_e = \frac{c}{2\sin(\theta/2)} \cdot \frac{\Delta\lambda_{1/e}}{\lambda_i} \tag{2.24}$$

Equation 2.24 substituted in equation 2.22 eventually gives an expression of T_e as a function of the half one–over–e width $\Delta\lambda_{1/e}$

$$T_e = \frac{m_e c^2}{8\sin^2(\theta/2) k_b \lambda_i^2} \cdot (\Delta\lambda_{1/e})^2 \tag{2.25}$$

With $\theta = 90^0$ this gives $T_e = 5243.68 \cdot (\Delta\lambda_{1/e})^2$ where $\Delta\lambda_{1/e}$ in nm.

b. $\alpha \leq 0.3$ (collective effects).

We see that now the scattered spectrum has the shape of a corrected Gaussian according to equation 2.20. This is shown in figure 2.7b for $\alpha = 0.3$.

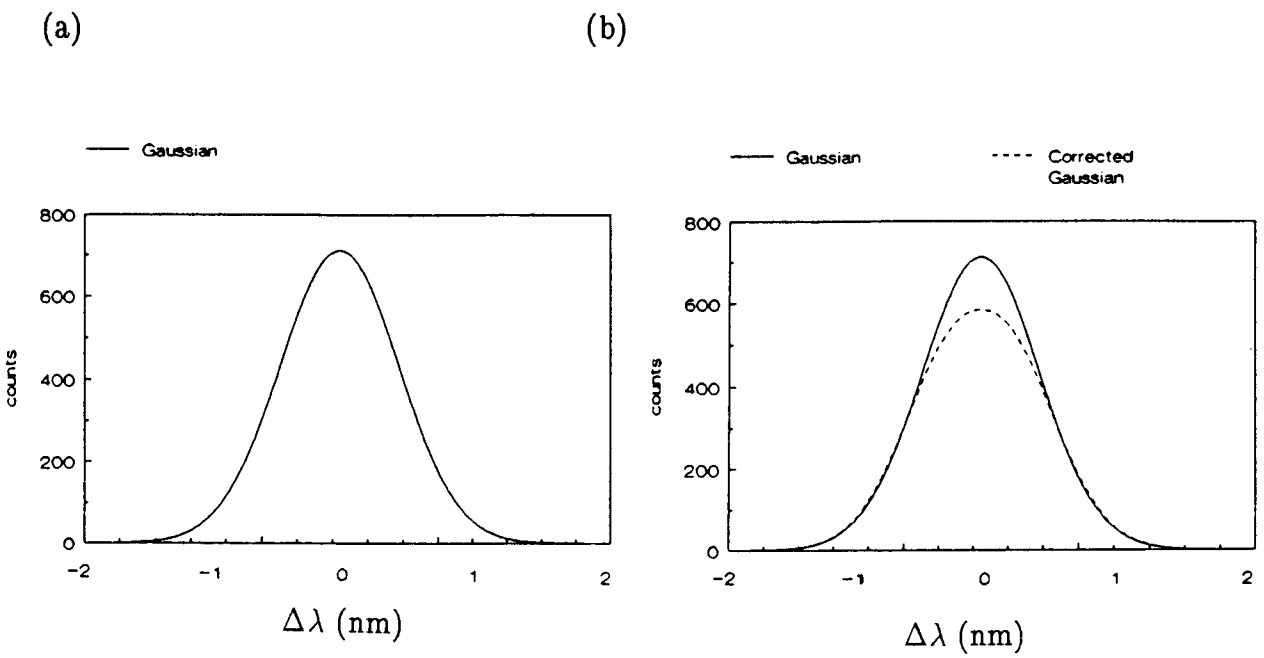

Figure 2.7 *The scattered spectrum around incident wavelength λ_i for incoherent scattering (a) and $\alpha = 0.3$ (b).*

We see in the above figure that the scattered signal is depressed in the center and broadend in the flanks of the spectrum in comparison with a true Gaussian. This leads of course to somewhat different values of T_e and n_e. If α is not too large (0.3) T_e will be smaller and n_e larger in comparison with analysis assuming incoherent scattering. The exact equation to calculate n_e is given in paragraph 3.4.

2.5 Rayleigh scattering

We now consider the scattering of electromagnetic radiation by bounded electrons of neutral atoms and ions, which is called *Rayleigh scattering*. The expression for the scattered power for Rayleigh scattering is similar to the one for Thomson scattering: equation 2.8, with n_e replaced by $n_0 + \beta^2 n_i$. β^2 Is the ratio between the differential cross sections of the ions (i) and neutrals (n). For Argon [8]:

$$\frac{d\sigma_{r,i}/d\Omega}{d\sigma_{r,n}/d\Omega} = \beta^2 = 0.393 \qquad (2.26)$$

The scattered power is given by

$$P_s d\omega_s = P_i \cdot (n_0 + \beta^2 n_i) \cdot L \cdot \Delta\Omega \cdot S(\mathbf{k},\omega)_r \cdot d\sigma_r/d\Omega \cdot d\omega_s \qquad (2.27)$$

with $d\sigma_r/d\Omega$ the differential cross section for Rayleigh scattering. The ratio of the differential Rayleigh and Thomson cross sections for Argon, for an incident wavelength of 532 nm (the Rayleigh cross section is, in contrast with the Thomson cross section, wavelength dependent), is [8]

$$\frac{d\sigma_r/d\Omega}{d\sigma_t/d\Omega} = \frac{1}{143} \qquad (2.28)$$

The Doppler width of the scattered spectrum is proportional to $m^{-1/2}$, with m in this case the mass of the atoms, so the width of the profile is negligible small compared to Thomson scattering, which means

$$\int_{-\infty}^{\infty} S(\mathbf{k},\omega)_r d\omega_s = \int_{-\infty}^{\infty} \delta(\omega) d\omega = 1 \qquad (2.29)$$

with $\delta(\omega)$ the Dirac delta function.

The scattered spectrum in the scattering experiments is thus a combination of scattering by free and bounded electrons. In figure 2.8 a simulation of a scattering experiment is given (see also chapter 4).

So from the scattered spectrum we can determine the electron density, electron temperature and the neutral density, with the equations derived in this chapter.

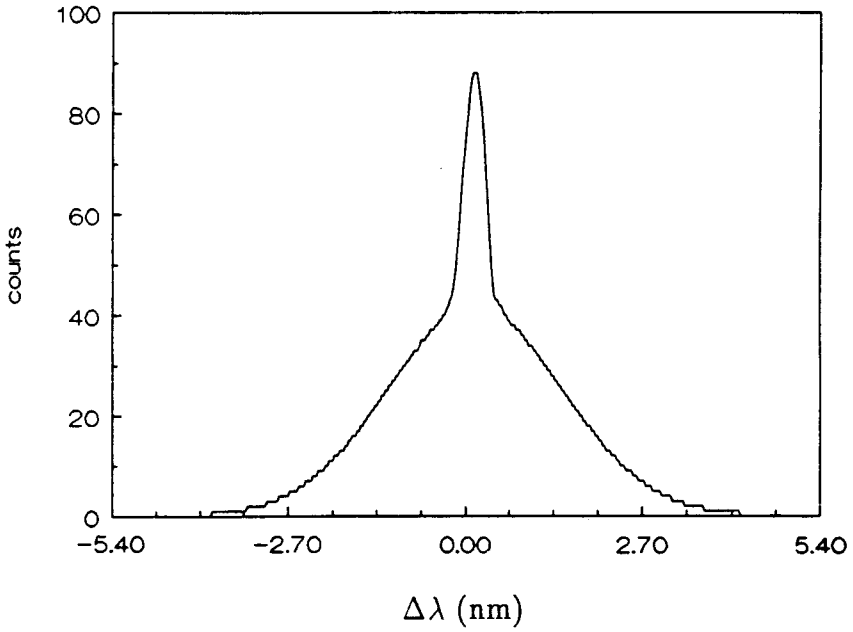

Figure 2.8 *Simulation of a Thomson scattering measurement ($n_e = 5 \cdot 10^{19}$ m^{-3}, $n_0 = 1 \cdot 10^{21}$ m^{-3} and $T_e = 17406.7$ K).*

2.6 Efficiency of Thomson scattering

The differential cross section for Thomson scattering is in the classical limit

$$d\sigma_t/d\Omega = r_e^2 \cdot (1 - \sin^2\theta \cos^2\phi_0) \tag{2.30}$$

where r_e is the classical electron radius:

$$r_e = \frac{e^2}{4\pi\epsilon_0 m_e c^2} = 2.81 \cdot 10^{-15} \text{ m} \tag{2.31}$$

So, in our case where $\theta = \phi_0 = 90^0$, we get

$$d\sigma_t/d\Omega = 7.9 \cdot 10^{-30} \text{ m}^2 \tag{2.32}$$

The ratio of the integrated scattered power and the incident power (see equation 2.8) gives the efficiency. The result is (including collective effects)

$$\frac{P_s}{P_i} = n_e \cdot (1 - \alpha^2) \cdot L \cdot \Delta\Omega \cdot d\sigma_t/d\Omega \qquad (2.33)$$

where $d\sigma_t/d\Omega$ from equation 2.32, L = 1 mm and $\Delta\Omega = 0.021$ sr. With $n_e = 1 \cdot 10^{20}$ m^{-3} and $\alpha = 0.2$ we get

$$\frac{P_s}{P_i} \approx 10^{-14}$$

which means that on 10^{14} incident photons only one is scattered. This means that for performing Thomson scattering, a high energy laser is necessary.

In this chapter we derived the basic equations to calculate from the scattering experiments the plasma parameters n_e, n_0 and T_e. In the next chapter we discuss the experimental set up, on which the scattering experiments are performed.

3 Experimental set up

3.1 Introduction

The cascaded arc set up is shown in figure 3.1. The three most important parts of this set up are:

- the plasma source, a cascaded arc;
- the vacuum vessel, into which the plasma expands;
- the diagnostics.

A plasma, generated by the cascaded arc, expands into the vessel (1) at low pressure (0.01 – 1 torr). To reach low pressure, different pumps are used: two fore pumps, three roots pumps (capacity 400, 1000 and 2000 m^3/hr) and two diffusion pumps.
The length of the plasma column is equal to the distance between the anode plate of the cascaded arc and the end anode both connected with the electrode support system (2). The vessel is surrounded by eight Helmholtz coils (3) which can apply a magnetic field parallel to the plasma jet.

In this chapter we discuss the cascaded arc briefly in paragraph 3.2, the Thomson–Rayleigh scattering diagnostics (4) in paragraph 3.3 and the calibration methods applied in this diagnostics in paragraph 3.4. Finally the effect of the laser on the plasma is discussed in paragraph 3.5.

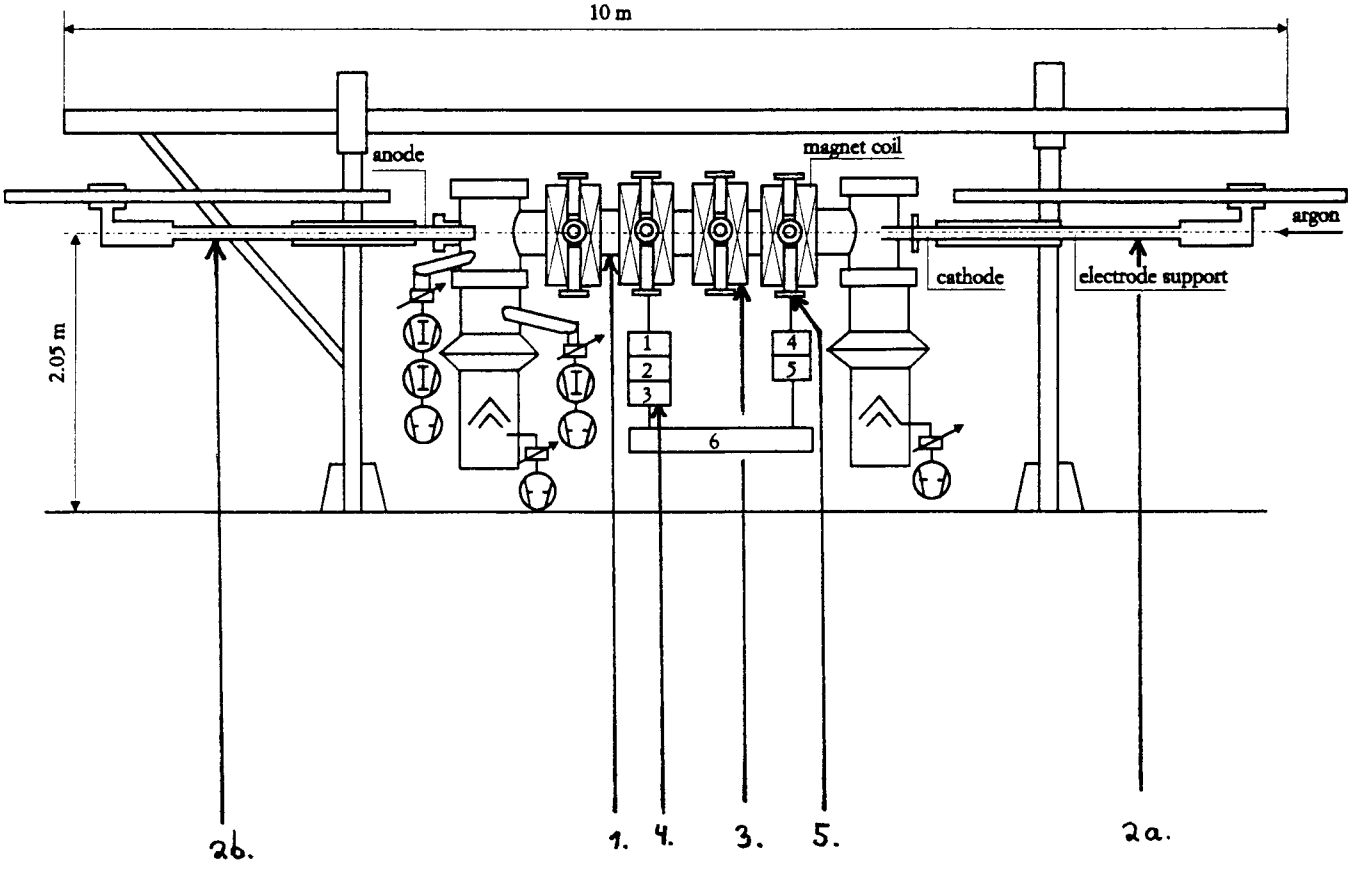

Figure 3.1 The general plasma set up.

1. *Vessel*
2. *Electrode support system: a. cascaded arc, b. end anode*
3. *Magnetic coils (water cooled)*
4. *Diagnostics*
5. *Viewing ports*

3.2 The plasma source

As a plasma source a wall stabilized arc is used (see figure 3.2). It consist of three tungsten–thorium cathodes, eight copper plates (which are electrically insulated from each other) and an anode plate. They are all water cooled. A voltage is applied between the cathodes and the anode of the cascaded arc. Argon gas is injected in the central channel of the arc. The gas is (partly) ionized by discharge between the cathodes and the anode plate. In this way a plasma is created which expands into the vacuum vessel. Plasma parameters as electron density n_e, electron temperature T_e, neutral density n_0 and heavy particle temperature T_h depend on the argon gas flow through the cascaded arc, the current between the cathode and the anode and the pressure. The plasma conditions used in this work are listed in table 3.1.
It is also possible to apply an additional voltage between the cathodes of the cascaded arc and the end anode. The used electrical configurations are shown in figure 3.3. For a more complete survey of the cascaded arc and the possible electrical circuits see [9].

Table 3.1 The plasma conditions used in the scattering experiments.

carrier gas	argon
gas flow	3500 ml/min
nozzle	4 mm
$p_{background}$	0.3 torr
$L_{plasma\ jet}$	700 mm
I_{casc}	45 A
$I_{plasma\ jet}$	0 – 45 A
I_B	0 – 360 A
V_{casc}	145 V
$V_{plasma\ jet}$	0 – 170 V
B	0 – 0.2 T

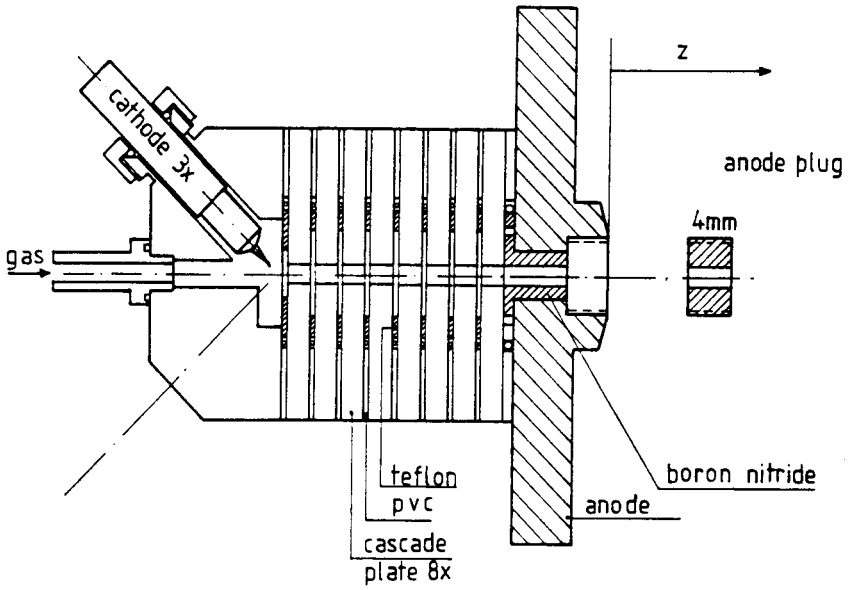

Figure 3.2 The cascaded arc.

(a) (b)

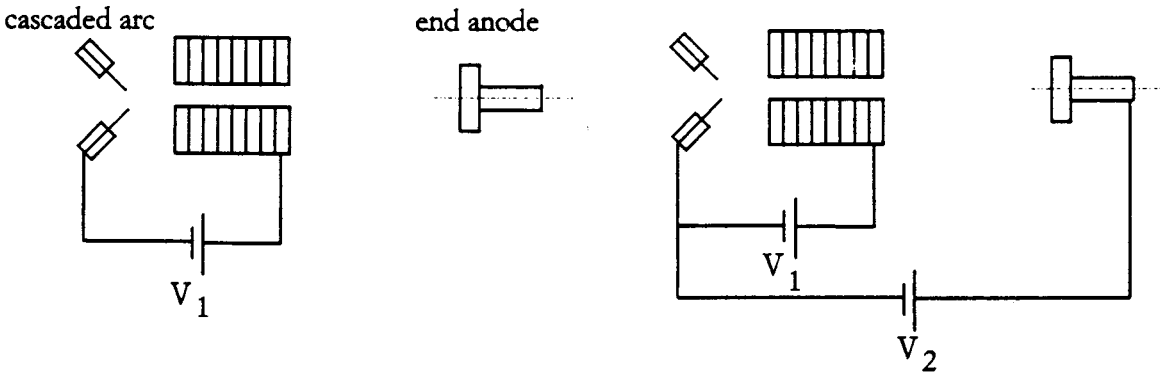

Figure 3.3 *The electrical circuit connected with the cascaded arc and the end anode; (a) the driving voltage is applied between the cathodes and the anode of the cascaded arc, the end anode is electrically isolated; (b) the cascade arc operates as described in (a) with an additional voltage applied between the cathodes of the cascaded arc and the end anode.*

3.3 The Thomson–Rayleigh scattering set up

At the position of viewing port nr 3 in figure 3.1 the experimental set up for Thomson–Rayleigh scattering is positioned. It is shown in detail in figure 3.4. The position of the scattering plane is normal to the axis of the plasma jet.

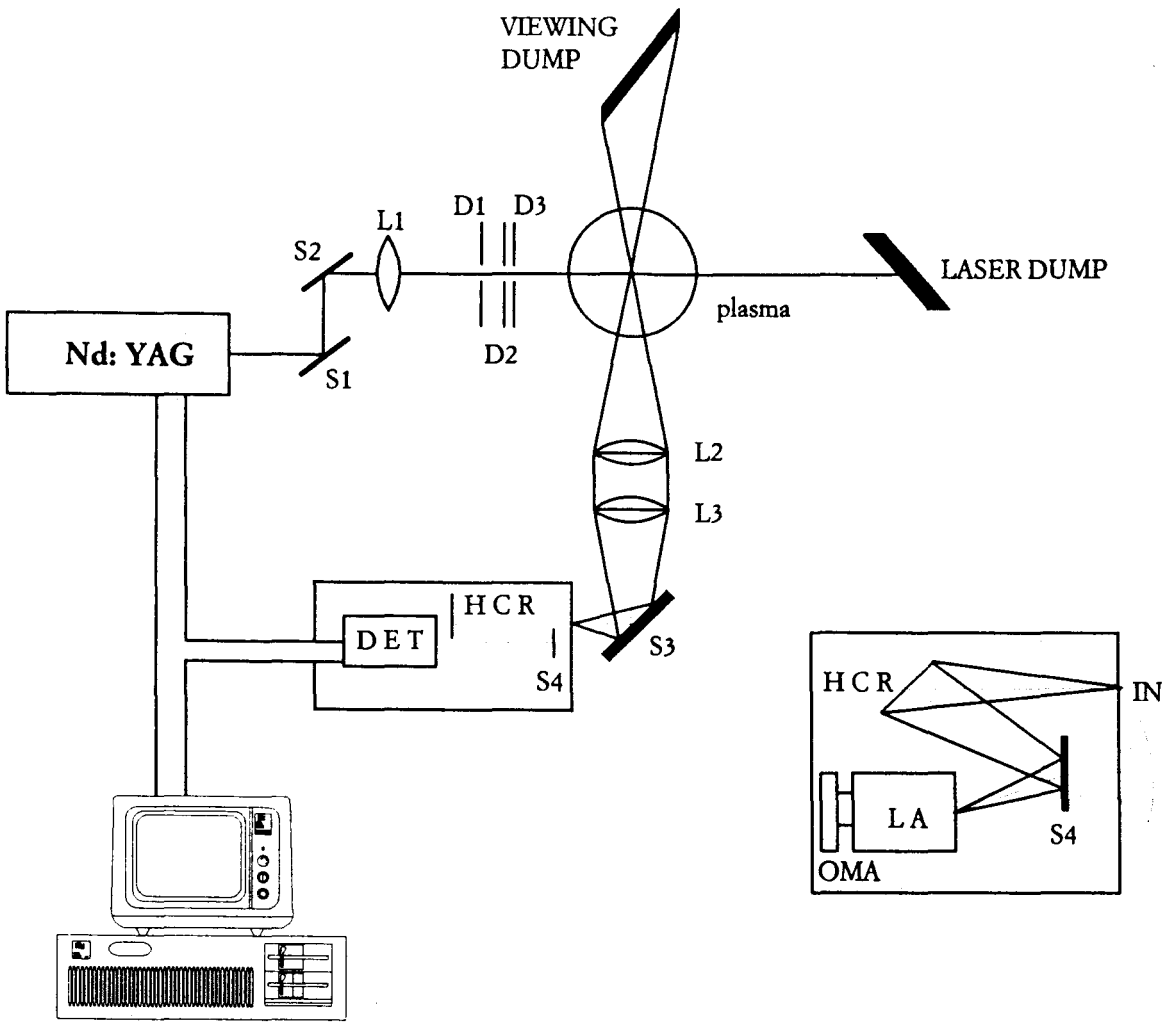

Figure 3.4 *The experimental set up for Thomson–Rayleigh scattering experiments (explanation see text).*

In figure 3.5 the cross section of the vessel is shown in more detail.
As a light source a frequency doubled Nd:YAG laser is used (DCR 11 Quanta Ray, wavelength 532 nm, energy per pulse E = 0.15 J/pulse, pulse width τ = 8 ns and repetition frequency f_{rep} = 10 Hz, further specifications are given in [10]). The laser light passes two dichroic mirrors S_1 and S_2 to separate the second harmonic from the first harmonic, which is dumped behind S_1 and S_2. After this the laser light is focused in the plasma, to a waist of 0.5 mm by lens L_1 (f = 500 mm). In the vessel tube T_1 several diaphragms are installed (D_1, D_2 and D_3) to diminish the stray light originating from laser light scattering at the entrance window W_1 of the vessel. In the tube T_2 opposite to the entrance window a laser dump is installed, which absorbs the incident laser light. This dump consists of a glass plate NG3 under the Brewster angle.

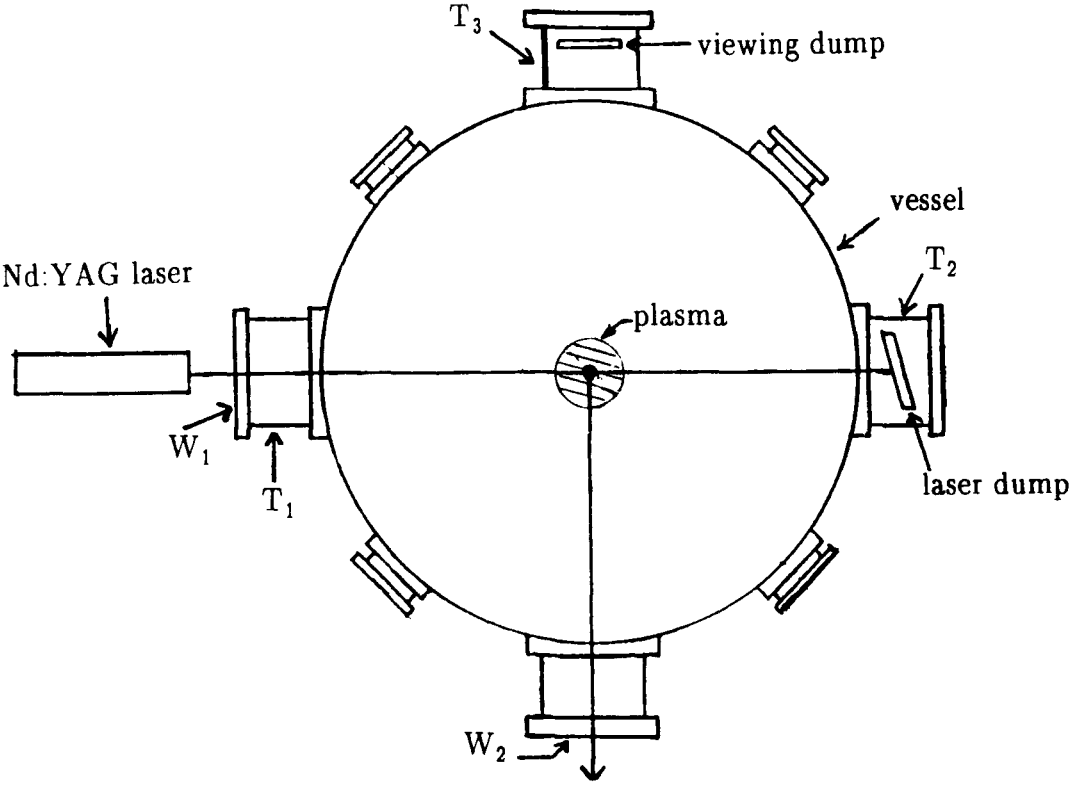

Figure 3.5 *Cross section of the vacuum vessel, at the position of the Thomson–Rayleigh scattering set up (viewing port nr 3).*

The 90^0 scattered light is observed through window W_2 and imaged one to one on the entrance slit of the polychromator by two plano convex lenses L_2 and L_3 (both with f = 500 mm) and a mirror S_4. In the tube T_3 opposite to the exit window a viewing dump is installed to reduce the stray light from that direction.

The polychromator consists of a holographic concave grating (HCR) and a detector. The HCR (special Jobin Yvon, 1800 lines/mm, Rowland geometry, radius of Rowland circle 500 mm, calculated dispersion on Rowland circle 1.11 nm/mm) disperses the scattered light (wavelength selection). A solid angle of $2.5 \cdot 10^{-2}$ sr is reached by matching the aperture ratio of lenses L_2 and L_3 to the aperture ratio of the HCR. The entrance and exit angles of the polychromator are chosen such to achieve minimal astigmatism on the Rowland circle for the used laser wavelength of 532 nm.

The detector consists of three parts: a gateable light amplifier (LA), an optical multichannel analyzer (OMA) and a personal computer (PC) with an ADC plug in unit. The photocathode (S2O, quantum efficiency 12 % at 532 nm) of the LA (Fiber Optic array, amplification 10^4, gating time τ_{gate} = 20 ns) is positioned on the Rowland circle. Light which strikes the photocathode is amplified. The LA is gated with a pulse generator which is triggered by the laser. Gating is necessary to minimize the plasma light during a measurement. The amplified Thomson–Rayleigh signal is detected with the OMA, which integrates the scattered signal during 1200 shots. It consists of a photo diode array PDA (1024 pixels: width 25 μm, height 2.5 mm, EG&G Reticon photo diode array RL1024S). The pixels are cooled with two peltier elements, which makes long integration times possible [1]. With an ADC converter the analog signal is digitized inside the personal computer PC. In this way the scattered signal is measured in ADC counts. One ADC count corresponds to 3.4 photons according to [11].

With the diagnostics discussed, Thomson–Rayleigh scattering measurements can be performed in expanding cascaded arc plasmas in axial and radial direction. For this the position of the plasma can be changed by moving the cascaded arc and the end anode independently in axial and/or radial direction. This has the advantage that the optics remains fixed. For definition of the axial and radial directions in the plasma see figure 3.6.

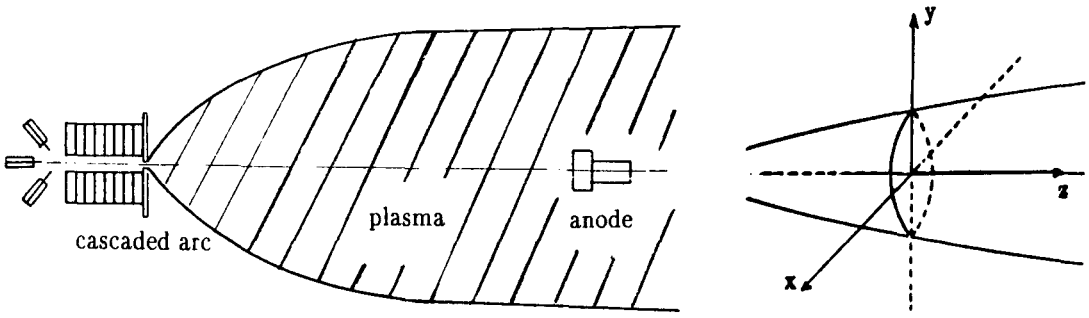

Figure 3.6 Definition of axial and radial directions in the expanding plasma.

3.4 Calibration methods

To determine correctly the three plasma parameters n_e, n_0 and T_e from the Thomson–Rayleigh scattering measurements, three different calibrations have to be performed. First an absolute calibration, to calculate the electron and neutral density, second a wavelength calibration, to calculate the electron temperature and third a relative calibration, to calibrate the different sensitivity of the pixels.

3.4.1 Absolute calibration

To calculate the electron and neutral density from the measured spectrum an absolute calibration is performed. It consists of a Rayleigh scattering measurement (on pure argon gas at a pressure of approximately 1.6 torr) under the same conditions as the Thomson–Rayleigh scattering measurements.
The neutral density $n_{0,cal}$ corresponding to this Rayleigh calibration measurement is calculated from

$$p = n_{0,cal} k_b T \tag{3.1}$$

where p = 1.6 torr and T = 296 K (room temperature). The accuracy in the measured pressure and temperature influences of course the calibration.

The ratio of the integrated signal of the Thomson component of the measured spectrum and the integrated Rayleigh scattering signal now gives the value of the electron density n_e. For pure argon gas the integrated Rayleigh scattering signal is (see chapter 2)

$$I_{cal} = \int_{-\infty}^{\infty} P_{s,c} d\omega_s = P_i \cdot n_{o,cal} \cdot L \cdot \Delta\Omega \cdot d\sigma_r/d\Omega \cdot T_{det} \qquad (3.2)$$

where T_{det} is the product of the transmission of the used optical components and the detection efficiency.
The integrated signal of the Thomson component of the measured spectrum is (including collective effects)

$$I_{thom} = \int_{-\infty}^{\infty} P_{s,t} d\omega_s = P_i \cdot n_e(1-\alpha^2) L \cdot \Delta\Omega \cdot d\sigma_t/d\Omega \cdot T_{det}' \qquad (3.3)$$

Because the Thomson and Rayleigh scattering measurements are done under the same conditions, i.e. $T_{det} = T_{det}'$, n_e is given by

$$n_e = \frac{I_{thom}}{I_{cal}} \cdot \frac{n_{o,cal}}{1-\alpha^2} \cdot \frac{d\sigma_r/d\Omega}{d\sigma_t/d\Omega} \qquad (3.4)$$

In the same way the ratio of the integrated signal of the Rayleigh component of the measured spectrum and the integrated signal of the Rayleigh calibration measurement gives the neutral density.
The integrated signal of the Rayleigh component of the measured spectrum is

$$I_{rayl} = \int_{-\infty}^{\infty} P_{s,r} d\omega_s = P_i(n_o+\beta^2 n_i) L \cdot \Delta\Omega \cdot d\sigma_r/d\Omega \cdot T_{det}' \qquad (3.5)$$

With I_{cal} from equation 3.2, $n_i = n_e$ (quasi neutrality) and $T_{det} = T_{det}'$, n_o is given by

$$n_o = n_{o,cal} \cdot \frac{I_{rayl}}{I_{cal}} - \beta^2 n_e \qquad (3.6)$$

where n_e is calculated from equation 3.4.

3.4.2 Wavelength calibration

The wavelength calibration is performed to calculate the electron temperature, which is proportional to the square of the width of the Thomson component of the measured spectrum (equation 2.24). Therefore the pixels of the OMA have to be calibrated with wavelength. This is done by measuring the spectra of some gas discharge lamps. We used Ne, Hg, Cs, Ar, Xe and Ti gas discharge lamps and the Nd:YAG laser. Afterwards the observed spectral lines are identified with wavelength. The result of the wavelength calibration is shown in figure 3.7.
As can be seen in this figure, a linear relation exists between wavelength and pixel number. From a least mean square fit we find

$$\lambda = a_0 + a_1 \cdot \text{pixel number} \tag{3.7}$$

where λ in nm, $a_0 = 517.3 \pm 3.0$ nm and $a_1 = 0.02684 \pm 0.007$ nm/pixel. The correlation $r = 0.9991$.

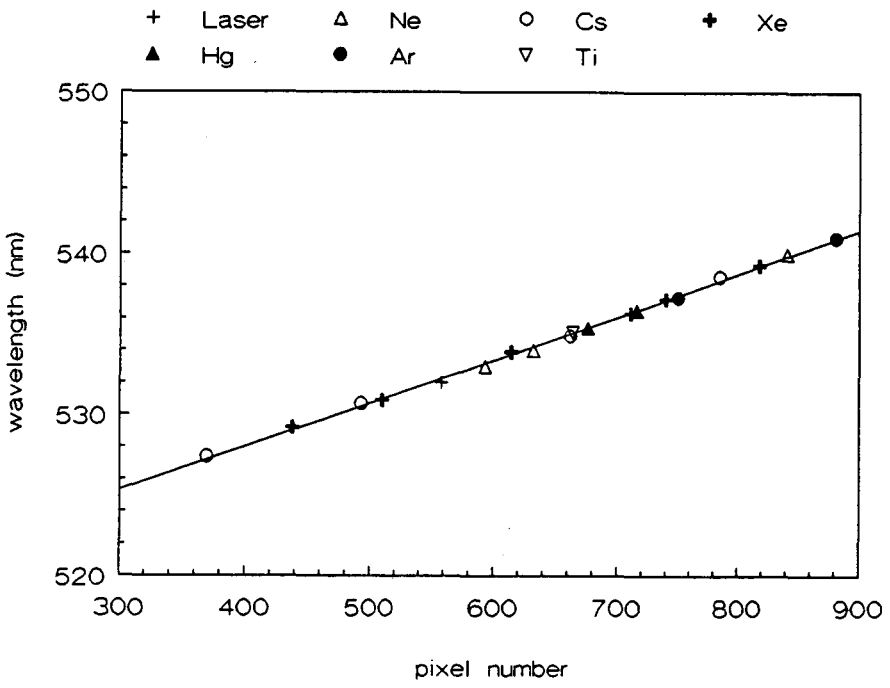

Figure 3.7 Wavelength calibration of the pixels.

3.4.3 Relative calibration

Calibration of the pixel sensitivity is performed with a tungsten ribbon lamp (Osram, type 17/G, nr. 1252, calibration certificate nr. 723.0307) under the same conditions as the Thomson–Rayleigh scattering measurements. The spectrum of the tungsten ribbon lamp is measured at one particular current through the ribbon (the radiance depends on the temperature of the ribbon and thus depends on the current through the ribbon, we choose a current of 14.00 ± 0.01 A). The measured spectrum is shown in figure 3.8. With the method described by [12] we can calculate the relative calibration. The Turbo Pascal programs "T_rad", "T_waar" and "Radiant" (all written by M.C.M. van de Sanden) are used for this aim.

Shortly the procedure is as follows:

- With "T_rad" the radiation temperature (at a current of 14 A) is calculated from the specifications given by the calibration certificate.
- From the radiation temperature the true temperature of the ribbon is calculated with "T_waar".

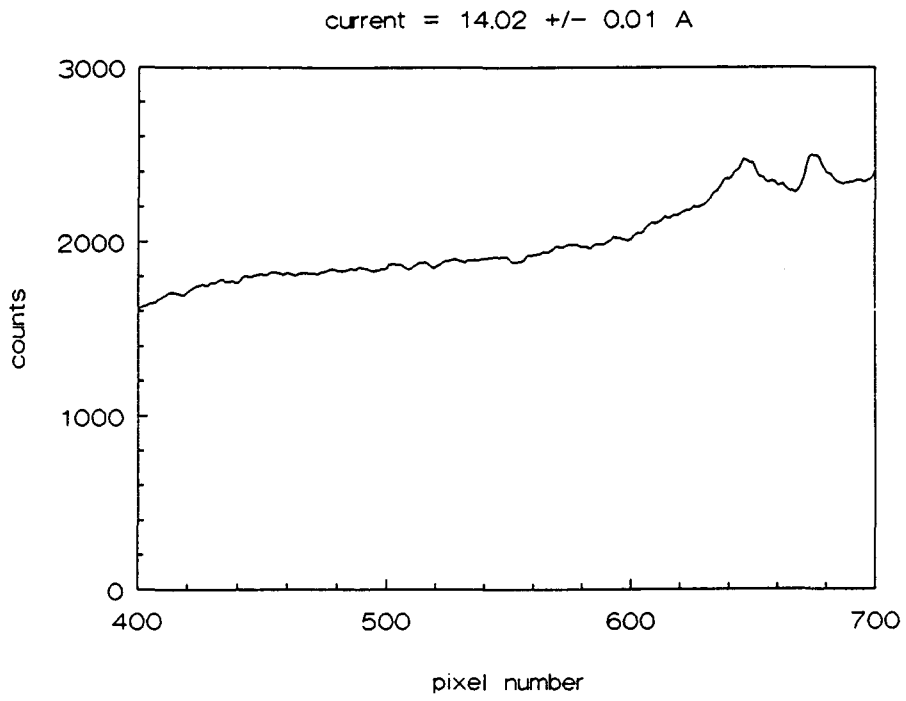

Figure 3.8 The measured tungsten ribbon lamp spectrum.

- The intensity for a few wavelengths at one true temperature is calculated with "Radiant". By fitting the result with a polynomial of order 3 we get the intensity as a function of wavelength at one true temperature (belonging to a current of 14 A).
- From the wavelength calibration, discussed in paragraph 3.4.2, we know the pixel numbers corresponding to the different wavelengths. So the relative calibration for each pixel can be calculated by dividing the tungsten ribbon lamp measurement by the calculated intensity.

Together with the absolute calibration (described in paragraph 3.4.1) and the wavelength calibration (described in paragraph 3.4.2) the measured Thomson–Rayleigh scattering measurements can be analyzed.

3.5 Influence of the laser on the plasma

In this paragraph we discuss two possible, laser induced, effects on the plasma. First heating of the plasma in subsection 3.5.1 and second disturbance of the plasma by the incident electric field in subsection 3.5.2.

3.5.1 Heating of the plasma by absorption of laser energy

An important restriction to the used laser is that it should not disturb the plasma. Absorption of the laser energy by the plasma can give rise to an increase of the electron temperature (inverse Brehmstrahlung). The laser energy can disturb the plasma also in other ways, here we discuss only the heating of the plasma by absorption of laser energy by the electrons. The increase is given by [8]:

$$\frac{\Delta T_e}{T_e} = 9.11\cdot 10^{-14}\frac{n_i Z^2}{(k_b T_e)^{3/2}}\cdot\frac{g_{ff}}{v^3}\cdot\left[1-\exp\left[-\frac{h v}{k_b T_e}\right]\right]\cdot\frac{1}{q}\cdot\int_0^{t_L} L\,dt \qquad (3.8)$$

where $n_i = n_e$, $Z = 1$, gaunt factor $g_{ff} = 1$, cross section of the laser beam in the plasma $q = \pi\cdot(0.25\cdot 10^{-3})^2 = 1.96\cdot 10^{-7}$ m^2, laser power $L = 1.88\cdot 10^7$ J/s, frequency of the laser fotons $v = c/\lambda_i = 5.64\cdot 10^{14}$ s^{-1} and time t_L between τ_{ee} and τ_{ei}, where τ_{ee} and τ_{ei} are the relaxation times for electron – electron and electron –ion momentum exchange. We take the upper limit $t_L = \tau_{ei} = 2.76\cdot 10^5\cdot T_e^{3/2}/(n_e \ln\Lambda_c)$. For $n_e = 5\cdot 10^{19}$ m^{-3} and $T_e =$ 2500 K we get $t_L = 1.28\cdot 10^{-10}$ s and $\Delta T_e/T_e = 4.86\cdot 10^{-5}$ which means that the increase

of the electron temperature, due to absorption of laser energy, is 0.12 K for $T_e = 2500$ K. This justifies the conclusion that heating of the plasma by absorption of laser energy can be neglected.

3.5.2 Disturbance of the plasma by the incident electric field

The incident electric field should be small enough not to disturb the plasma, i.e. the acceleration during one cycle of the electric field should be smaller than the thermal speed in the scattering plane. This requires

$$v_e = \frac{eE_i}{m_e\omega_i} \ll v_{th,e} = \left[\frac{2k_bT_e}{m_e}\right]^{1/2} \tag{3.9}$$

where $\omega_i = 2\pi c/\lambda_i = 3.54 \cdot 10^{15}$ s^{-1}. The electric field is related to the incident power per unit area by

$$\frac{P_i}{A} = \tfrac{1}{2}\epsilon_0 E_i^2 \cdot c \tag{3.10}$$

where $A = 1.96 \cdot 10^{-7}$ m^2 the cross section of the laser in the plasma. With substitution of equation 3.10 in equation 3.9 we get the condition

$$\frac{P_i}{A} \ll \frac{m_e\omega_i^2 k_b T_e \epsilon_0 c}{e^2} = 1.63 \cdot 10^{13} \cdot T_e \tag{3.11}$$

with T_e in K. For the Nd:YAG laser used in this work we find $P_i/A = 9.59 \cdot 10^{13}$ Js^{-1}m^{-2}. So for $T_e = 2500$ K and all the electron temperatures measured in this work (1500 – 20000 K) the conclusion is justified that the influence of the incoming electric field is negligible.

4 Analysis methods of scattering measurements

4.1 Introduction

To calculate the electron density n_e, electron temperature T_e and the neutral density n_o from the scattering measurements a fit program has been developed. This program uses a non–linear least mean square fit method based on the Levenberg–Marquardt algorithm [14]. In paragraph 4.2 the theory of this fitting method is described. For all programming details of the fit program, the reader is referred to the user guide [15]. Paragraph 4.3 treats the possible components of the model function, used in the fit program (described in paragraph 4.2). Several tests performed on the fit program are explained and discussed in paragraph 4.4.

4.2 Least mean square fit procedures with nonlinear models

We consider a model $y = y(x,\mathbf{a})$ which depends nonlinearly on a set of M unknown parameters a_k, $k = 1...M$. With this model we want to fit a set of N data points (x_i,y_i). Usually $N > M$. We define the Chi Square function χ^2, which measures the agreement between the data and the nonlinear model with a particular choice of the set of parameters $\mathbf{a}$, as

$$\chi^2(\mathbf{a}) = \sum_{i=1}^{N} \left[\frac{y_i - y(x_i,\mathbf{a})}{\sigma_i} \right]^2 \qquad (4.1)$$

with y_i the i^{th} data point, $y(x_i,\mathbf{a})$ the value of the model function at x_i and σ_i the standard deviation (uncertainty) of y_i.
We determine the best fit parameters by minimization of χ^2. Close to the minimum the χ^2 function can be approximated by its Taylor series:

$$\chi^2(\mathbf{a}) \approx \gamma - \mathbf{d}\cdot\mathbf{a} + \tfrac{1}{2}\mathbf{a}\cdot\mathbf{D}\cdot\mathbf{a} \qquad (4.2)$$

with γ a constant: $\gamma \equiv \chi^2(\mathbf{a}_{min})$, $\mathbf{d}$ is an M–vector: $\mathbf{d} \equiv -\nabla\chi^2(\mathbf{a})|_{\mathbf{a}_{min}}$ and $[\mathbf{D}]_{ij} \equiv \partial\chi^2(\mathbf{a})/\partial a_i \partial a_j|_{\mathbf{a}_{min}}$, a M×M matrix (D is called the Hessian matrix: the second partial derivative matrix of the χ^2 function at $\mathbf{a}_{min}$).
From equation 4.2 the gradient of χ^2 is calculated as

$$\nabla\chi^2(\mathbf{a}) = \mathbf{D}\cdot\mathbf{a} - \mathbf{d} \tag{4.3}$$

Here we made use of the fact that $\mathbf{D}\cdot\mathbf{a} = \mathbf{a}\cdot\mathbf{D}$. The gradient vanishes at $\mathbf{a}_{min}$ obtained from

$$\mathbf{D}\cdot\mathbf{a}_{min} = \mathbf{d} \tag{4.4}$$

At the current point $\mathbf{a}_{cur}$ we have

$$\mathbf{D}\cdot\mathbf{a}_{cur} = \nabla\chi^2(\mathbf{a}_{cur}) + \mathbf{d} \tag{4.5}$$

So when our current approximation $\mathbf{a}_{cur}$ is a good one (which means that $\mathbf{a}_{min} - \mathbf{a}_{cur}$ is the finite step we have to take to reach the exact minimum), we get by subtracting of equation 4.5 from equation 4.4

$$\mathbf{D}\cdot(\mathbf{a}_{min} - \mathbf{a}_{cur}) = -\nabla\chi^2(\mathbf{a}_{cur}) \tag{4.6}$$

On the other hand it is also possible that at $\mathbf{a}_{cur}$ equation 4.2 is a poor local approximation to the shape of the function $\chi^2(\mathbf{a})$ that we are trying to minimize at $\mathbf{a}_{cur}$. In this case we take a step down the gradient $\nabla\chi^2(\mathbf{a}_{cur})$. This is called the *steepest descend method*:

$$\mathbf{a}_{next} = \mathbf{a}_{cur} - \text{constant}\cdot\nabla\chi^2(\mathbf{a}_{cur}) \tag{4.7}$$

where the constant is small enough not to exhaust the downhill direction.
To find $\mathbf{a}_{min}$ with equations 4.6 and 4.7 we have to know the Hessian matrix D and the gradient of χ^2. We can calculate these two because we know the exact form of χ^2 (equation 4.1).

a. The gradient of χ^2 with respect to a_k is:

$$\frac{\partial \chi^2}{\partial a_k} = -2 \sum_{i=1}^{N} \left[\frac{y_i - y(x_i,\mathbf{a})}{\sigma_i} \right] \cdot \frac{\partial y(x_i,\mathbf{a})}{\partial a_k} \tag{4.8}$$

with k = 1...M.

b. The components of the Hessian are the second partial derivatives of χ^2:

$$\frac{\partial^2 \chi^2}{\partial a_k \partial a_l} = 2 \sum_{i=1}^{N} \frac{1}{\sigma_i^2} \cdot \left[\frac{\partial y(x_i,\mathbf{a})}{\partial a_k} \cdot \frac{\partial y(x_i,\mathbf{a})}{\partial a_l} - [y_i - y(x_i,\mathbf{a})] \cdot \frac{\partial^2 y(x_i,\mathbf{a})}{\partial a_l \partial a_k} \right] \tag{4.9}$$

We now define:

$$\beta_k = -\tfrac{1}{2} \frac{\partial \chi^2}{\partial a_k} \tag{4.10}$$

and the curvature matrix $[\alpha]$ with components:

$$\alpha_{kl} = \tfrac{1}{2} \frac{\partial^2 \chi^2}{\partial a_k \partial a_l} = \tfrac{1}{2} D \tag{4.11}$$

We see from equation 4.10 that at the minimum $\beta_k(a_{min}) = 0$ for all k.
From equation 4.9 and 4.11 we see that α_{kl} depends on both the first and second derivatives of the model function with respect to its parameters. We ignore in further discussion the second derivative term because of the following reasons:

- The second derivative term is zero in the linear case.
- When it is small enough compared to the first derivative term, it can be neglected: for a good model the term $[y_i - y(x_i,\mathbf{a})]$ in equation 4.9 should be the random measurement error of each data point (positive or negative), which is not correlated to the model. So the summation over i of the second derivative multiplied with $[y_i - y(x_i,\mathbf{a})]$ should give zero.

Now we can write equation 4.6 and 4.7, with substitution of α_{kl} and β_k defined in equation 4.10 and 4.11, as

$$\sum_{l=1}^{M} \alpha_{kl} \cdot \delta a_l = \beta_k \tag{4.12}$$

respectively

$$\delta a_l = \text{constant} \cdot \beta_l \tag{4.13}$$

with δa_l the increment $\mathbf{a}_{next} - \mathbf{a}_{cur}$ added to the current approximation $\mathbf{a}_{cur}$.
We know already that equation 4.12 is used close to the minimum and equation 4.13 far from the minimum. Marquardt managed to combine the two equations in one equation as follows:
First we look at the constant in equation 4.13. Considering dimensions the constant should have a dimension of a_k^2, because χ^2 is nondimensional (see equation 4.1) and β_k has therefore a dimension of $1/a_k$.
When we now look at the curvature matrix $[\alpha]$ (equation 4.11) we see that only one quantity exists with a dimension of a_k^2: $1/\alpha_{kk}$ (the components of the curvature matrix $[\alpha]$ have dimensions $1/a_k a_l$). So this quantity should set the scale of the constant.
We additionally divide the constant by a nondimensional factor λ because $1/\alpha_{kk}$ may be too big. So equation 4.13 now becomes

$$\delta a_l = \frac{1}{\lambda \alpha_{ll}} \cdot \beta_l \tag{4.14a}$$

or

$$\lambda \alpha_{ll} \cdot \delta a_l = \beta_l \tag{4.14b}$$

Notice that α_{ll} is always positive (equation 4.9 with the second derivative term set to zero).

Now we can combine equation 4.12 and 4.14b when we define a new matrix $[\alpha']$ with components:

$$\alpha_{jj}' \equiv \alpha_{jj}(1 + \lambda)$$

$$\alpha_{jk}' \equiv \alpha_{jk} \qquad (j \neq k) \tag{4.15}$$

So the final equation is:

$$\sum_{l=1}^{M} \alpha_{kl}' \cdot \delta a_l = \beta_k \tag{4.16}$$

At the limit $\lambda \rightarrow 0$ we get back equation 4.12 and at $\lambda \rightarrow \infty$ (α' diagonally dominant) we get back equation 4.14b.
Briefly, the Levenberg–Marquardt method is shown in a flow chart in figure 4.1.

Remarks:

- The minimization is ready when the stop condition is satisfied: if in n following iterations the decrease in $\chi^2(\mathbf{a})$ is less than 0.1, stop iterating: the stop condition n has to be given by the user.
- When the minimization is fulfilled the covariance matrix $[C] = [\alpha]^{-1}$ is calculated. The diagonal elements C_{jj} of the covariance matrix give the squared uncertainties of the fitted parameters **a**. We use as uncertainty of the fitted parameters the Root Mean Square deviation, defined as:

$$\sigma_{\text{effective,j}} = \sqrt{\frac{\text{chi square}}{N - M} \cdot C_{jj}} \tag{4.17}$$

for parameter a_j.
The off–diagonal elements C_{jk} ($j \neq k$) give the covariance of parameter a_j with parameter a_k.

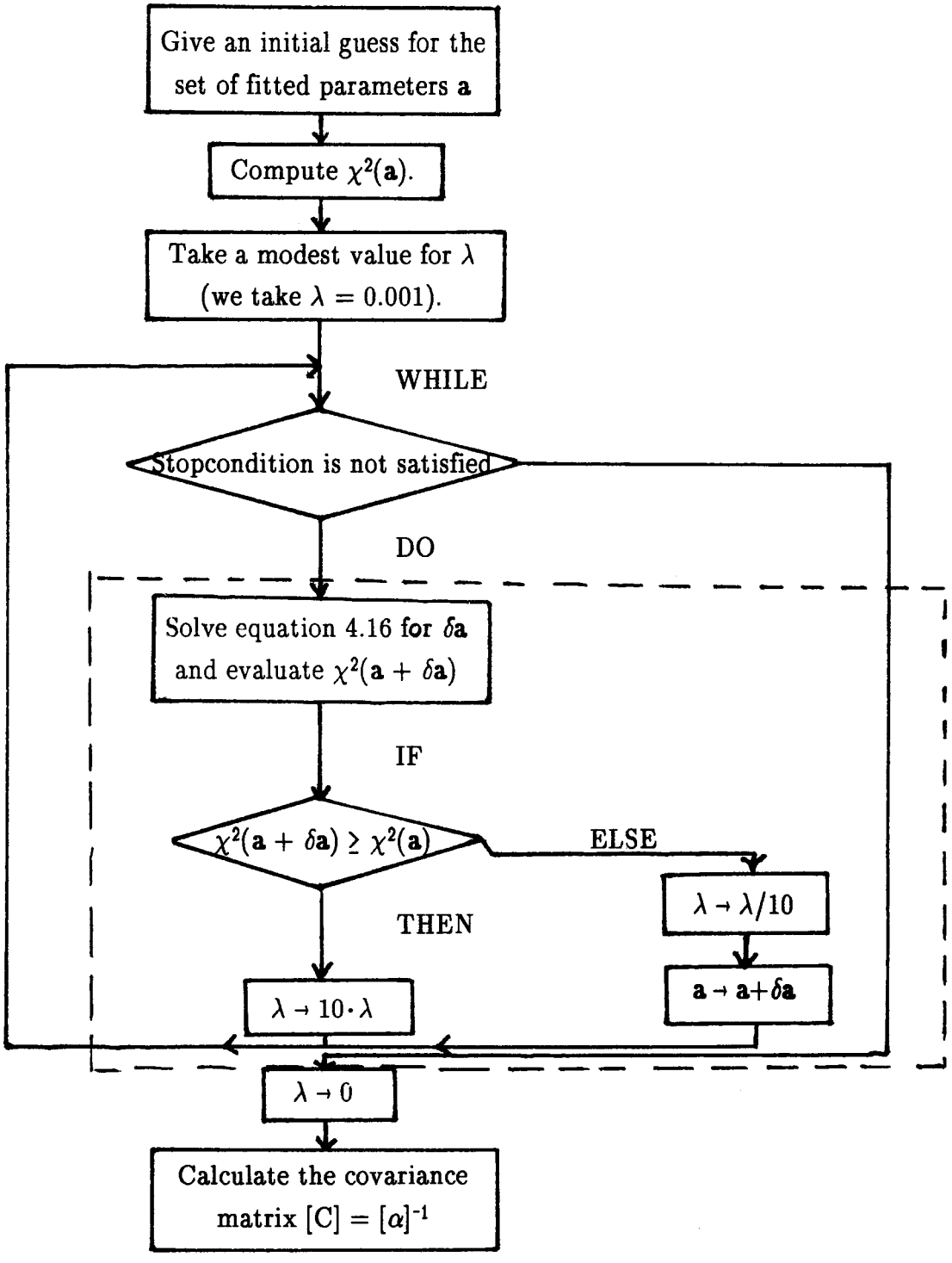

Figure 4.1 *Flow chart of the Levenberg–Marquardt fit method. The box indicates one iteration.*

We say that a measurement is fitted well if the value of the minimized χ^2 function is in the order of N – M, with N – M the degrees of freedom of the system. N is the total amount of data points and M the total amount of parameters of the model function. The measurement errors are normally distributed, with the measurement error of one data point

$$\sigma_i = \left[\frac{y_i}{3.4} \right]^{1/2} \tag{4.18}$$

where the factor 3.4 arises because the photons obey the $\sqrt{N}$ statistics and one ADC count corresponds to 3.4 photons [11].

- An other method to say something about the quantity of the fit is looking at the autocorrelation *ac* of the residue (measurement – fit) [16]. *ac* Is a number between –1 and +1. If *ac* is zero then the residue is uncorrelated, if it is 1 (or –1) the residue is completely correlated. We say that no systematics occurs in the residue, when *ac* is approximately between –0.3 and +0.3. In this case the correct model functions are used.

In the next paragraph we discuss an explicit expression for the model function used to fit the scattering measurements with the analysis method here described.

4.3 The model function to be used in the scattering experiments

In general a scattering measurement consist of three components:

- a background;
- a Thomson component, which is a convolution of the true Thomson component with the apparatus profile;
- a Rayleigh component, which has the shape of the apparatus profile.

Logically, the model function $y(x,\mathbf{a})$ which is used to fit the measurements should consist of three similar components. Here x is the wavelength and **a** the parameter set used in the model function. The possible components of the model function are:

1 a linear background:

$$y(x) = a_0 + a_1 \cdot x \tag{4.19}$$

where a_0 is the offset and a_1 is the slope. Because the cooling of the pixels is not constant, measurements do not have the same background. These differences are taken into account by the linear background.

2 a Gaussian (used in the case of incoherent scattering):

$$y(x) = \frac{a_0}{a_2\sqrt{\pi}} \cdot \exp\left[-\left[\frac{x - a_1}{a_2}\right]^2\right] \tag{4.20}$$

where a_0 is the surface sum, a_1 is the position and a_2 is the half one–over–e width of the Gaussian.

3 a Gaussian corrected for collective effects (used in the case where α is not very small):

$$y(x) = \frac{a_0}{a_2\sqrt{\pi}} \cdot \exp\left[-\left[\frac{x - a_1}{a_2}\right]^2\right] \cdot \left[1 - 2\alpha^2 \cdot \mathrm{Rw}\left[\frac{x - a_1}{a_2}\right]\right] \tag{4.21}$$

where a_0, a_1 and a_2 are the same as in 2 and $\mathrm{Rw}\left[\frac{x - a_1}{a_2}\right]$ is the real part of the plasma dispersion function given by equation 2.14. Notice that the scattering parameter α is a function of a_0 and a_2.

4 a measured component which reflects the scaled apparatus profile:

$$y(x) = a_0 \cdot f(x - a_1) \tag{4.22}$$

where a_0 is a multiplier, a_1 is a shift in position and f(x) is the measured profile. In our case f(x) is a measured apparatus profile.

The possible convolution of the function y(x) given in equations 4.20 or 4.21 with an apparatus profile a(x) is calculated using Fast Fourier Transforms [14]. We call the result s(x):

$$s(x) = y(x) \times a(x) = \int_{-\infty}^{+\infty} a(x_a) \cdot y(x - x_a) dx_a \tag{4.23}$$

The model function is now a combination of the components given above. The fit program is tested by fitting some simulations with different model functions. This is described in the next paragraph.

4.4 Testing the fit program

In this paragraph we test the fit program. In subsection 4.4.1 we examine the apparatus profile. In subsections 4.4.2 and 4.4.3 tests for incoherent scattering respectively collective effects are discussed.

4.4.1 About the apparatus profile

A Rayleigh scattering measurement (which has a very small Doppler width) is broadend to an apparatus profile of finite width, because the entrance slit of the polychromator is not infinitely small. A Rayleigh scattering measurement, done under the same measuring conditions as the Thomson–Rayleigh scattering measurements is shown in figure 4.2. The only differences in the conditions are the used pressure of 1.6 torr (background pressure in the vessel) compared with 0.3 torr for the Thomson–Rayleigh scattering measurements and the gas temperature. We tested if the shape of the Rayleigh scattering measurement changes under different pressures. Therefore Rayleigh scattering

measurements were performed under three different pressures, namely 0.3 torr, 1.6 torr and 100 torr. From the results we can say that the shape of the Rayleigh scattering measurements does not change under different pressures.

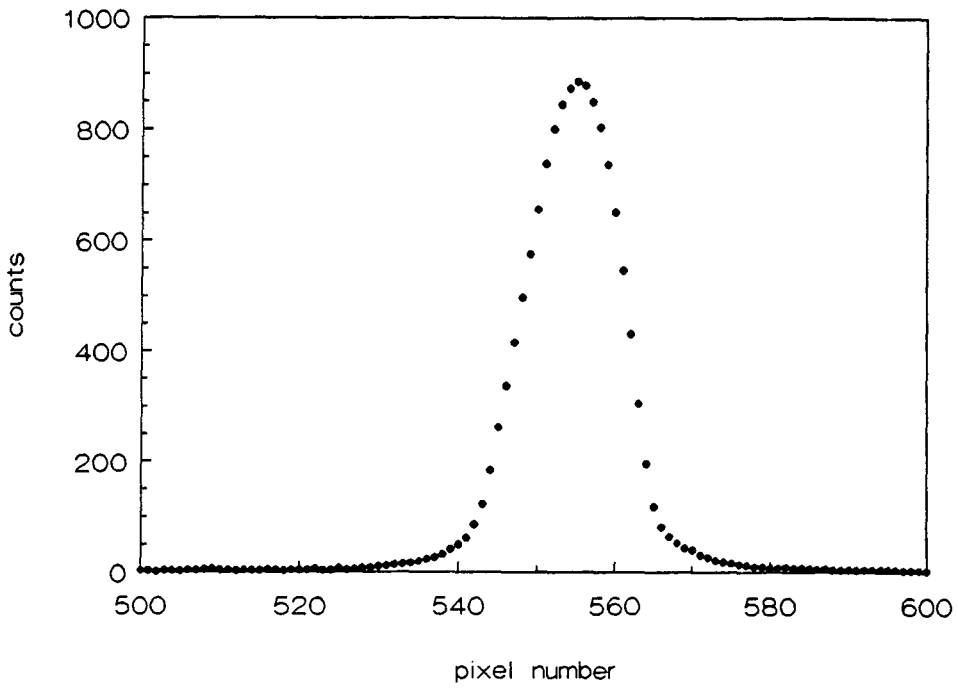

Figure 4.2 A Rayleigh scattering measurement which serves as apparatus profile.

Examination of the above figure shows that the apparatus profile has an asymmetric shape. We fitted the apparatus profile with a model function consisting of a varying amount of Gaussians (1 – 3). The only reasonable fit was made by using a model function which contained three Gaussians. Unfortunately the positions of the Gaussians are such that, physically spoken, no conclusions can be drawn from this result. In practice it means that, first, the Rayleigh component of a scattering measurement can only be fitted well with a profile with the same shape as the apparatus profile, i.e. a scaled Rayleigh scattering measurement. Second, the Thomson component of a scattering measurement, which is a convolution of the true Thomson component with the apparatus profile (normalized on a surface sum of one), can only be fitted well when the convolution is calculated with the real apparatus profile and not with a simplification as for example a Gaussian. This is made plausible in the next two subsections.

4.4.2 Tests for incoherent scattering

Six simulations of scattered spectra are made. They are all build up of a Gaussian (nr. 2 in paragraph 4.3) convoluted with a measured apparatus profile plus a scaled apparatus profile (nr. 4 in paragraph 4.3). The first component reflects the Thomson component and the second component the Rayleigh component of the scattered spectrum. The parameters of the simulations are adjusted to the values of the electron temperature T_e and electron density n_e given in table 4.1. T_e is proportional to the square of the half one–over–e width and n_e is proportional to the surface sum of the Gaussian. The neutral density n_0 is for all simulations the same ($1 \cdot 10^{21}$ m^{-3}). In figure 4.3 a picture of the six simulations is shown. The chosen values of n_e, n_0 and T_e are values which are to be expected in the Thomson–Rayleigh scattering experiments.

Table 4.1 Simulations of scattered spectra ($n_0 = 1 \cdot 10^{21}$ m^{-3}).

Simulation	n_e (m^{-3})	T_e (K)
1	$5 \cdot 10^{18}$	5802.23
2		17406.68
3	$5 \cdot 10^{19}$	5802.23
4		17406.68
5	$5 \cdot 10^{20}$	5802.23
6		17406.68

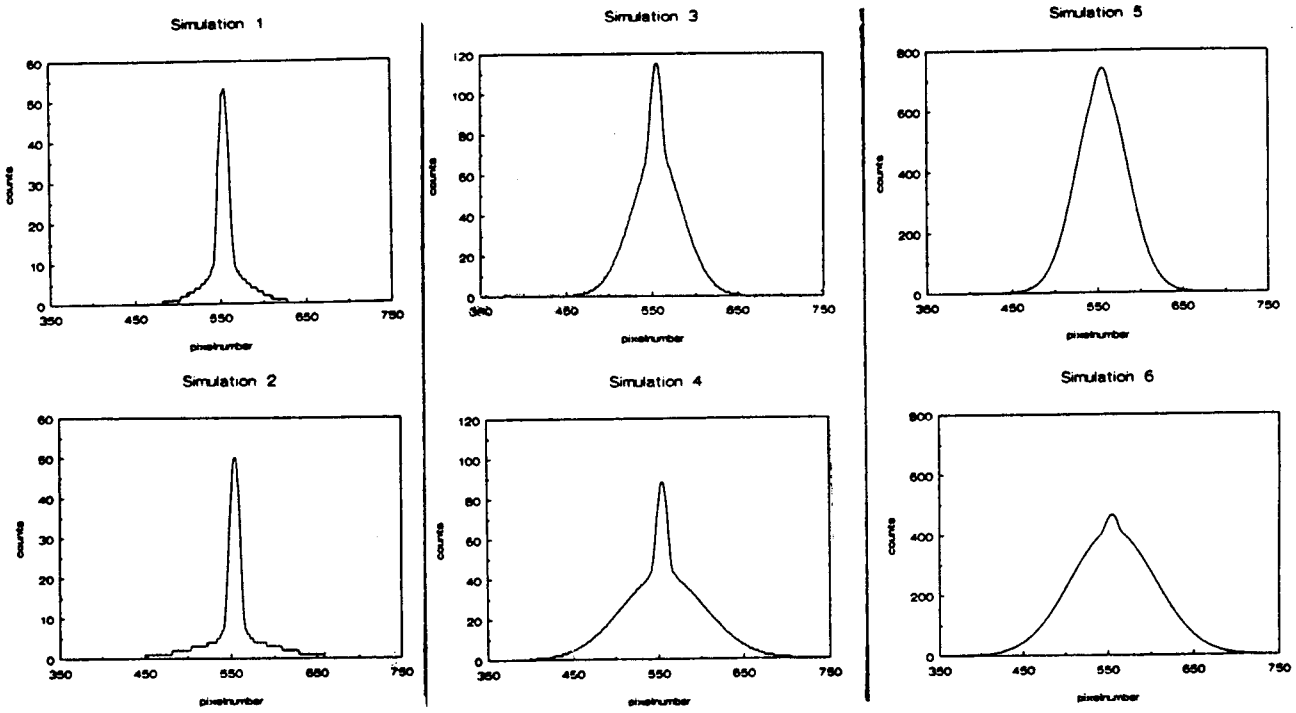

Figure 4.3 Simulations of scattered spectra according to table 4.1.

The simulations are fitted in three different ways, with model functions with components:

- a background plus two Gaussians;
- a background plus a Gaussian plus a scaled apparatus profile;
- a background plus a Gaussian convoluted with a measured apparatus profile plus a scaled apparatus profile.

What is our aim to fit the simulations in these ways?

1 Examine if the three different fitting methods give essential differences in the estimation of the plasma parameters n_e, n_0 and T_e with regard to each other and in comparison with the simulations.

2 Examine the time scale on which the three fitting methods operate.

We will see that large differences occur between the three fitting methods.

1 The estimation of n_e, n_0 and T_e

The results of the different fitting methods are listed in table 4.2 on the next page. From the table we can draw the following conclusions:

- Examining the relative differences of the plasma parameters between fit and simulation for the three methods, we see that the relative differences for method 3 are significantly smaller than those of method 1 and 2. For electron densities of $5 \cdot 10^{19}$ m^{-3} and higher the difference between method 1 and 2 compared to method 3 becomes quite clear. Method 3 then gives within 1 % the correct values of the plasma parameters in contrast with the first two methods. These methods give considerable differences compared with the correct values from the simulations. Apparently these methods can not clearly distinguish the Thomson and Rayleigh component from each other when n_e becomes of the order of n_0. See the picture of simulation 5 in figure 4.3.
- For very low values of n_e ($5 \cdot 10^{18}$ m^{-3}) the results of the fits for method 3 are less good then for higher n_e values.
- From table 4.2 it is not so that simulations with smaller T_e are better (or worse) fitted than simulations with higher T_e. To see this, compare the results of simulations 1 and 2, 3 and 4, 5 and 6 with each other. The cause is that for smaller T_e the Thomson and Rayleigh components become more difficult to distinguish from each other.
- The most difficult simulation to fit is simulation 2, where n_e is very low and T_e is high. The relative differences in the plasma parameters between fit and simulations are in the order of 10 % for all three fitting methods. We see from the picture of simulation 2 in figure 4.3 that the Thomson component is so low that pixels close to each other have the same amount of counts. The large relative differences are then caused by round off errors. Fortunately, in our scattering experiments we do not come even close to this situation of very low n_e and high T_e.

From these conclusions we can say that the best fitting method is method 3, where the model function consists of a background plus a Gaussian convoluted with an apparatus profile plus a scaled apparatus profile. We have to notice also that the relative differences between fit and simulation decrease with larger n_e. So if n_e is large the plasma parameters n_e, n_0 and T_e are determined more accurate.

Table 4.2 *Fit results for the six simulations in the case of incoherent scattering (The relative differences are differences with regard to the true values of the simulations.).*

Simulation 1	method 1	method 2	method 3
$\Delta n_e/n_e$	8.4 %	1.2 %	0.49 %
$\Delta n_o/n_o$	7.4 %	0.2 %	0.095 %
$\Delta T_e/T_e$	8.5 %	10.0 %	2.2 %

Simulation 2	method 1	method 2	method 3
$\Delta n_e/n_e$	14 3 %	8.7 %	8.9 %
$\Delta n_o/n_o$	6.3 %	6.4 %	6.3 %
$\Delta T_e/T_e$	5.2 %	17.6 %	14.6 %

Simulation 3	method 1	method 2	method 3
$\Delta n_e/n_e$	0.24 %	0.45 %	0.16 %
$\Delta n_o/n_o$	2.2 %	2.7 %	0.79 %
$\Delta T_e/T_e$	11.0 %	10.7 %	1.7 %

Simulation 4	method 1	method 2	method 3
$\Delta n_e/n_e$	0.15 %	0.57 %	0.36 %
$\Delta n_o/n_o$	6.2 %	0.058 %	0.043 %
$\Delta T_e/T_e$	1.9 %	2.8 %	0.35 %

Simulation 5	method 1	method 2	method 3
$\Delta n_e/n_e$	40.8 %	0.66 %	0.10 %
$\Delta n_o/n_o$	2900 %	29.9 %	5.5 %
$\Delta T_e/T_e$	32.6 %	10.5 %	0.84 %

Simulation 6	method 1	method 2	method 3
$\Delta n_e/n_e$	0.13 %	0.20 %	0.009 %
$\Delta n_o/n_o$	4.6 %	1.6 %	0.63 %
$\Delta T_e/T_e$	3.4 %	3.4 %	0.29 %

2 Time scale on which the fitting methods operate

The time which is needed for the three methods to fit the simulations is shown in figure 4.4.

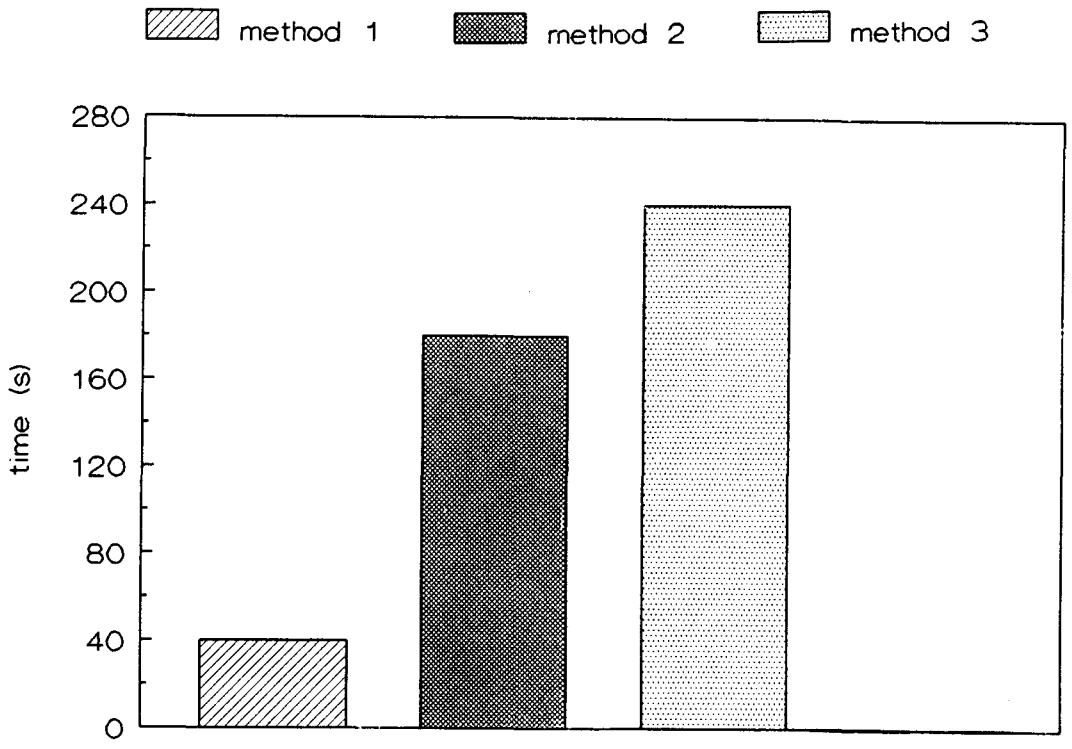

Figure 4.4 *Time scale on which the three fitting methods operate. The time shown is the time needed to perform ten iterations (see figure 4.1).*

The most simple form of fitting is method 1, where the only operation is adding the three components. In the second method, a scaled measured apparatus profile is shifted over the wavelength range to obtain a good fit. As it is a measurement, the apparatus profile forms a discrete spectrum. This makes the use of a cubic spline interpolation procedure necessary [14], which accounts for the extra calculation time. In method 3 in comparison with method 2, also a convolution is calculated using Fast Fourier Transforms [14]. This is the reason why this method is somewhat slower than method 2. Summed up, method 3 is the most accurate fitting method, especially at n_e values above $5 \cdot 10^{19}$ m^{-3} which is the case in almost all our scattering experiments. At the same time, however, method 3 is also the slowest fitting method. As the time scale, on which this

method operates, is not exceptional big and because we want to analyze our measurements as accurate as possible, we choose method 3 as fitting method for the scattering experiments.

4.4.3 Test for collective effects

A simulation of a scattering measurement is made including collective effects. It consists of a Gaussian corrected for collective effects (nr. 3 in paragraph 4.3) convoluted with a measured apparatus profile plus a scaled apparatus profile. The plasma parameters corresponding to this simulation are: $n_e = 1.7 \cdot 10^{20}$ m^{-3}, $n_0 = 3.6 \cdot 10^{21}$ m^{-3}, $T_e = 3400$ K and $\alpha = 0.195$.

The simulation is fitted in two ways, with model functions which consist of:

- a background plus a Gaussian convoluted with a measured apparatus profile plus a scaled apparatus profile;
- a background plus a Gaussian corrected for collective effects convoluted with a measured apparatus profile plus a scaled apparatus profile.

Again we examine the relative differences between the two fitting methods and the simulation and the time scale on which the methods operate.

1 The estimation of n_e, n_0 and T_e

The results of the two fitting methods are listed in table 4.3.

Table 4.3 *Fit results for the simulation in the case of collective effects (the variables are the same as in table 4.2).*

Simulation	method 1	method 2
$\Delta n_e/n_e$	2.8 %	0.033 %
$\Delta n_0/n_0$	6.4 %	0.56 %
$\Delta T_e/T_e$	3.6 %	0.13 %

Conclusions:

- Method 2 gives approximately 10 times smaller relative differences between fit and simulation than method 1.
- The improvements assert themselves in an increase in n_e and n_0 and a (small) decrease in T_e (in agreement with [2]). We can derive an general equation for the correction in $n_{0,I}$ as a function of $n_{e,II}$ and the correction in $n_{e,I}$:

$$\Delta n_0 = -\left[\frac{d\sigma_t/d\Omega}{d\sigma_r/d\Omega} + \beta^2\right] \cdot \Delta n_e + \alpha^2 \frac{d\sigma_t/d\Omega}{d\sigma_r/d\Omega} \cdot n_{e,II} \qquad (4.24)$$

where $\Delta n_e = n_{e,II} - n_{e,I}$ and $\Delta n_0 = n_{0,II} - n_{0,I}$. In figure 4.5 the correction Δn_0 is depicted versus $n_{e,II}$ for various Δn_e for $\alpha = 0.195$.

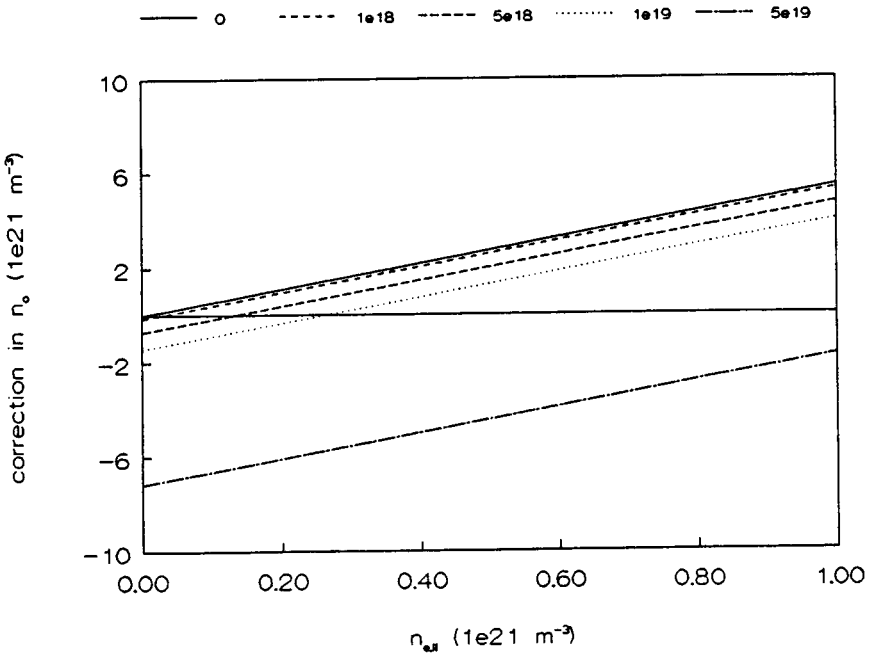

Figure 4.5 The correction in $n_{0,I}$ versus $n_{e,II}$ for various Δn_e.

It appears that the correction in $n_{0,I}$ can be appreciable in the parameter range of the expanding cascaded arc plasma even when $\Delta n_e = 0$, i.e. when the electron densities obtained by the two methods are the same.

- The scattering parameter α is deliberately chosen 0.195, a value which is very near to the α's in the scattering experiments. From table 4.3 and figure 4.5 we see that even for small α it is a significant improvement to use a model function which is corrected for collective effects.

2 Time scale on which the fitting methods operate

To correct a Gaussian for collective effects, an integral in the real part of the plasma dispersion function has to be calculated (see equation 2.14). This calculation comes on top of the other calculations already discussed in subsection 4.4.2. As a consequence the calculation time is increased. This is shown in figure 4.6.
As in subsection 4.4.2 we choose accuracy above speed and thus use method 2 to fit the scattering measurements.

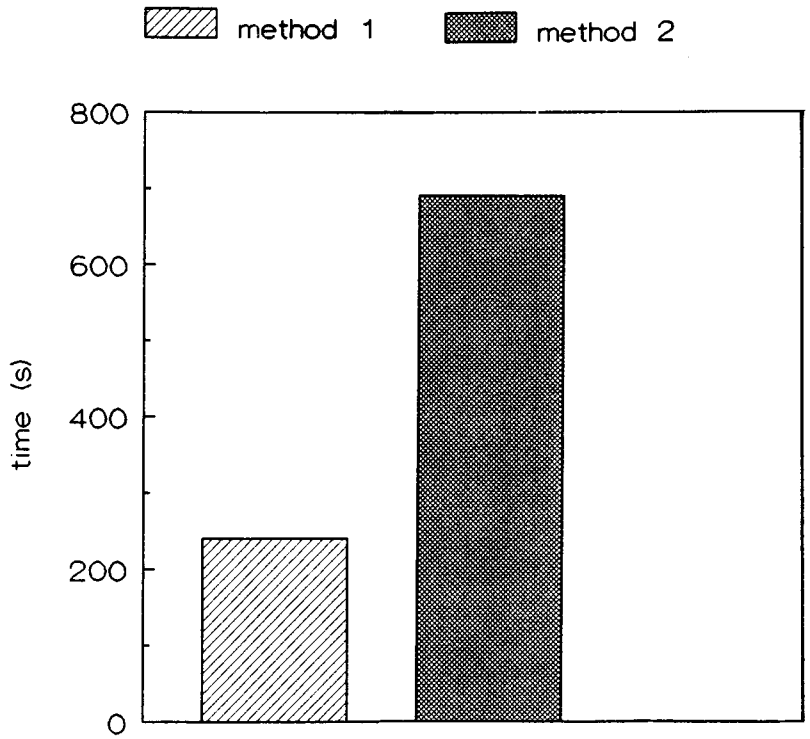

Figure 4.6 *Time scale on which the two fitting methods operate. The time shown is the time needed to perform ten iterations (see figure 4.1).*

5 Shock wave theory

In this chapter the theory of shock waves is treated shortly as an introduction on chapter 6, where the experimental results are discussed. For a more complete survey of shock waves see for example [17], [18], [19] or [20].
In paragraph 5.1 the Rankine–Hugoniot relations for a normal shock wave are treated. Paragraph 5.2 considers mean free paths because these determine the thickness of the shock. Also an expression for the position of the shock is given.

5.1 Rankine–Hugoniot relations for a normal shock wave

The laws of conservation of mass, momentum and energy form the basis for the equations of flow of a gas. These laws can be applied to flow regions where the variables undergo a discontinuous change. In our case the flow variables are the electron and heavy particle (neutral atoms and ions) temperatures, the electron and neutral densities and the electron and heavy particle temperatures.
A discontinuity can be regarded as the limiting case of very large but finite gradients in the flow variables, i.e. the flow variables change rapidly across a region which is usually very thin. Such discontinuities represent shock waves.
We apply the general laws of conservation of mass, momentum and energy to find the unknown flow variables. The conservation of mass, momentum and energy through a shock are described by the *Rankine–Hugoniot relations*. For a normal shock wave these relations read (without a magnetic field)

$$\rho_1 u_1 = \rho_2 u_2 \tag{5.1}$$

$$p_1 + \rho_1 u_1^2 = p_2 + \rho_2 u_2^2 \tag{5.2}$$

$$h_1 + \tfrac{1}{2} u_1^2 = h_2 + \tfrac{1}{2} u_2^2 \tag{5.3}$$

The left–hand side contains the flow variables in front of the shock and the right–hand side contains the flow variables behind the shock.

In equations 5.1 – 5.3 is ρ the mass density, u the velocity of the plasma, p the pressure and h the enthalpy:

$$\rho = m_o(n_e + n_o) \tag{5.4}$$

$$u = \frac{\Sigma n_x m_x w_x}{\Sigma n_x m_x} \approx w_h \tag{5.5}$$

where the subscript x denotes electrons, ions and neutrals and w_h is the velocity of the heavy particles (neutrals and ions). Here we assume that $w_i = w_o = w_h$.
An expression for the enthalpy is derived by [21]:

$$h = \frac{1}{\rho}\left[\frac{\gamma}{\gamma - 1}k_b(n_o + n_e)T_h + \frac{\gamma}{\gamma - 1}k_b n_e T_e + n_e E^{1+}\right] \tag{5.6}$$

where the ionization energy of the ground state $E^{1+} = 2.524 \cdot 10^{-18}$ J, the ratio of specific heats $\gamma = c_p/c_v$ and the assumption $T_i = T_o = T_h$ is made.
The equation of state is

$$p = \rho R(T_h + \alpha T_e) \tag{5.7}$$

where the gas constant $R = 8.315 \cdot 10^7$ Jmol^{-1}K^{-1} and the ionization degree $\alpha = \frac{n_e}{n_e + n_o}$.
It is useful to express the ratios of densities, velocities, pressures and temperatures in a shock wave in terms of the Mach number $M_1 = u_1/c_1$, where the velocity of sound is given by

$$c = \left[\gamma \frac{p}{\rho}\right]^{1/2} \tag{5.8}$$

With a shock wave, across which the gas is compressed, the gas flows into the shock with a supersonic velocity $u_1 > c_1$ ($M_1 > 1$) and flows out with a subsonic velocity $u_2 < c_2$ ($M_2 < 1$). With $\gamma = 5/3$ (for monatomic perfect gases) the following formulas can be derived from the above equations:

$$\rho_2 = \rho_1 \cdot (1 + 3/4 \cdot (1 - M_1^2)/M_1^2)^{-1} \tag{5.9}$$

$$u_2 = u_1 \cdot (1 + 3/4 \cdot (1 - M_1^2)/M_1^2) \tag{5.10}$$

$$p_2 = p_1 \cdot (1 + 5/4 \cdot (M_1^2 - 1)) \tag{5.11}$$

$$T_2 = T_1 \cdot (1 + 3/16 \cdot (5M_1^2/3 + 1)(M_1^2 - 1)/M_1^2) \tag{5.12}$$

where $T = T_h + \alpha T_e$.
Equations 5.9 – 5.12 show that the following inequalities are satisfied across a shock:

$$\begin{aligned} &\rho_2 > \rho_1 \\ &u_2 < u_1 \\ &p_2 > p_1 \\ &T_2 > T_1 \end{aligned} \tag{5.13}$$

Like the other variables the entropy S is discontinuous across the shock: $S_2 > S_1$.

5.2 Thickness and position of a normal shock

a Mean free paths for momentum and energy transfer between the particles in a plasma

The thickness of a shock is determined by the mean free paths for momentum exchange between electrons, ions and neutrals:

$$\lambda_{ei} = \tau_{ei} \cdot v_{th,e} \tag{5.14}$$

$$\lambda_{ii} = \tau_{ii} \cdot v_{th,i} \tag{5.15}$$

$$\lambda_{io} = \tau_{io} \cdot v_{th,i} \tag{5.16}$$

where τ_{ei}, τ_{ii} and τ_{io} are the relaxation times of momentum transfer between electrons and ions, ions and ions respectively ions and neutrals and the thermal velocity is $v_{th,x} = (3k_b T_x/m_x)^{1/2}$ for species e (electrons) or i (ions). The relaxation times are given by [22], [23]:

$$\tau_{ei} = 2.755 \cdot 10^5 \cdot \frac{T_e^{3/2}}{n_e \ln\Lambda_c} \tag{5.17}$$

$$\tau_{ii} = \left[\frac{m_i}{m_e}\right]^{1/2} \left[\frac{T_h}{T_e}\right]^{3/2} \cdot \tau_{ei} \tag{5.18}$$

$$\tau_{io} = 8.29 \cdot 10^{16} \cdot \frac{1}{n_o T_h^{1/2}} \tag{5.19}$$

where the Coulomb logarithm $\ln\Lambda_c = \ln(9n_e \cdot 4\pi\lambda_D{}^3/3)$ with the Debye length $\lambda_D = (\epsilon_0 k_b T_e / n_e e^2)^{1/2}$.

The mean free paths for energy exchange between electrons and ions and ions and neutrals are

$$\lambda_{ei}{}^{\epsilon} = \frac{m_i}{2m_e} \cdot \lambda_{ei} \tag{5.20}$$

$$\lambda_{io}{}^{\epsilon} = \lambda_{io} \tag{5.21}$$

Equations 5.20 and 5.21 give some information of the energy exchange between the particles behind the shock.

b Position of the shock

The position of the shock in the electron and neutral densities can be calculated with an empirical expression given by [24], [25]:

$$\frac{x_M}{d^*} = 0.67 \cdot \left[\frac{p_0}{p_\infty}\right]^{1/2} \tag{5.22}$$

where x_M is the location of the Mach–disk measured from the nozzle exit, d^* is the effective sonic nozzle diameter, p_0 the pressure at the nozzle exit and p_∞ the background pressure in the vessel. The Mach–disk forms the boundary between the adiabatic expansion and the shock.
Equation 5.22 describes the location of the Mach–disk measured from the nozzle exit for a free expanding plasma.
The shock wave theory treated in this chapter provides us with a basis to discuss the experimental results in chapter 6.

6 Experimental Results

In this chapter we discuss the results obtained from the experiments. First a general introduction is given in paragraph 6.1. Detection limits, accuracy and reproducibility of the scattering experiments are treated in paragraph 6.2, 6.3 and 6.4. The positions of the Thomson components of the measurements are considered in paragraph 6.5. Paragraph 6.6 treats the distribution of the Chi Squares of all the fitted measurements. Systematic differences between fits and measurements are discussed in paragraph 6.7. Finally measurements of the plasma parameters n_e, n_0 and T_e on the plasma axis are presented and discussed in paragraph 6.8.

6.1 General introduction

The Thomson–Rayleigh scattering measurements done in this work have to be corrected for stray light and calibrated before they are fitted by the developed fit program discussed in chapter 4.
First each scattering measurement is accompanied with a vessel stray light measurement. This vessel stray light is subtracted from the scattering measurement. Second on the resulting spectrum a relative calibration is performed.
In figure 6.1 the axial dependence of the vessel stray light is depicted for the free expanding plasma. As can be seen in the figure the vessel stray light increases exponentially close to the nozzle exit due to scattering of the laser light on the nozzle. On higher axial positions (50 mm and higher) the vessel stray light is approximately constant (900 counts). Clearly it is necessary to correct the scattering measurements for the vessel stray light.

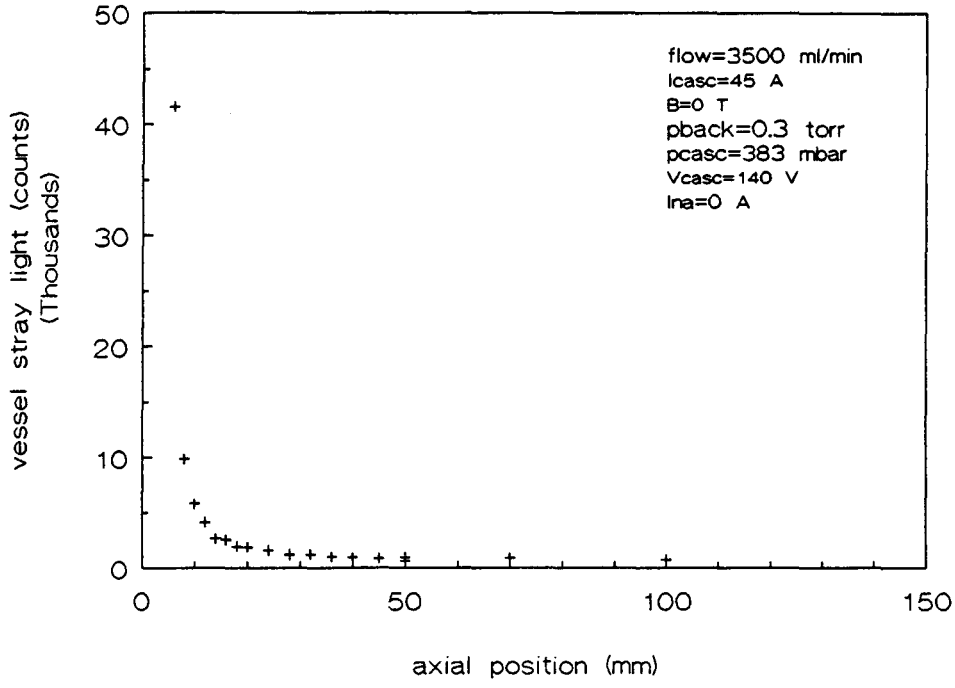

Figure 6.1 *The vessel stray light as a function of axial position for the free expanding plasma.*

Remarks:

- the vessel stray light does not have the same shape as the Rayleigh calibration measurements. This because the stray light comes from every corner of the vessel while the Rayleigh signal comes only from the laser bundle;
- although the vessel stray light is very high close to the nozzle exit, we managed to perform scattering measurements as close as 2 mm from the nozzle exit.

After this preparation the measurement is fitted with a model function consisting of

- a linear background;
- a convolution of a Gaussian, if necessary corrected for collective effects, and a measured apparatus profile. This component represents the Thomson component of a measurement;
- a scaled apparatus profile which represents the Rayleigh component of a measurement.

The apparatus profile which is used in the model function is a Rayleigh scattering measurement on pure Argon gas, performed under the same conditions as the Thomson–Rayleigh scattering measurements.

6.2 Detection limits

Measurements of the neutral density n_0 are limited by the amount of detected stray light. In our experiments the level of the vessel stray light is about 900 counts (see figure 6.1). The statistical error related to this level is 16 counts, which is much smaller than the reproducibility in the measured stray light (about 100 counts). Dust particles present in the low pressure vessel cause the difference between the statistical error and reproducibility. The latter sets the lower limit to measure n_0.
A reproducibility of 100 counts corresponds with an electron density of $9.8 \cdot 10^{17}$ m^{-3} and a neutral density of $1.4 \cdot 10^{20}$ m^{-3}. Here the difference between electron and neutral density is the relation between the differential cross sections for Thomson and Rayleigh scattering given by equation 2.28. The level of $1.4 \cdot 10^{20}$ m^{-3} with an accuracy of the same order makes it possible to measure neutral densities as low as $2 \cdot 10^{20}$ m^{-3} with an accuracy of 50 %. With the same accuracy electron densities as low as $1.3 \cdot 10^{18}$ m^{-3} can be measured.
The second factor which limits the accuracy in the determination of n_0 is the electron temperature, which is proportional to the square of the half one–over–e width of the Thomson component of a measured profile. With a constant electron density the higher the electron temperature the lower the contribution of the Thomson component to the total signal in the central channel. This lowers the statistical error of the signal in the central channel and thus leads to a higher accuracy in n_0.
The lower limit in the determination of the electron temperature is determined by the half one–over–width of the measured apparatus profile. In our experiments this width is about 16 pixels which corresponds to an electron temperature of approximately 1000 K.

6.3 Accuracy in the measurements

The errors in the plasma parameters n_e, n_0 and T_e can be divided in random and systematic errors.
The random error in the electron density is determined by:

- shot noise in the signal (following Poisson statistics);
- instrumental noise due to the laser and the detector (± 1 %);
- reproducibility of the plasma conditions (± 1 %).

The systematic error in n_e is determined by the relative and absolute calibrations. This error is approximately 2 %.

Reproducibility of the plasma conditions is determined by:

- current through the cascaded arc;
- current drawn from the cascaded arc to the end anode;
- strength of the applied magnetic field;
- pressure in the vessel;
- argon gas flow through the cascaded arc;
- cooling of the vessel;
- instabilities in the plasma.
- x, y, z position in the plasma.

For the neutral density the random error is determined by the same factors as for the electron density plus the accuracy in the vessel stray light signal. This last factor is the most important one as the accuracy in the stray light is determined by the reproducibility in the stray light. The systematic error is the same as for the electron density.

For the electron temperature the random error is determined by the accuracy in the width of the Thomson component of a measurement. The systematic error consists of

- the relative calibration;
- the wavelength calibration (± 1 %);
- the analysis method. This means analysis with or without convolution procedures.

The errors in n_e, n_0 and T_e resulting from the fitting of the measurements with the model function described in paragraph 5.1 is of the same order as the sum of random and systematic errors here discussed. For n_e the error is in the order of 1–4 % while the error in T_e is in the order of 2–4 %. For neutral densities above $2 \cdot 10^{20}$ m^{-3} the error is in the order of 10–20 %.

As the electron density is proportional to the surface sum under the Thomson component it is an integrated parameter. See also paragraph 3.4. This makes it reasonable accurate. The electron temperature depends on the square of the half one–over–e width of the Thomson component of a measurement and thus is not an integrated parameter. This explains why the error in T_e is bigger than the error in n_e.

Finally, when in the analysis procedure of the measurements no collective effects are included an extra systematic error in n_e, n_0 and T_e is introduced. The size of this error depends on the scattering parameter. For an idea of this error see sub paragraph 4.4.3.

6.4 Reproducibilities

The reproducibility of the measurements is determined by the laser, detector and the reproducibility of the plasma conditions. In this paragraph we discuss first the calibration measurements. Second the reproducibility in the scattering measurements is treated.

a Calibration measurements

As the absolute calibrations depend strongly on the laser energy, they have to be performed far more often than relative calibrations. So here we investigate only the absolute calibration measurements.
An absolute calibration is a Rayleigh scattering measurement on pure Argon gas under the same conditions as Thomson–Rayleigh scattering measurements. In paragraph 3.4.1 the principle of an absolute calibration is explained. From equation 3.4 and 3.6 we see that these equations can be written as

$$n_e = \frac{I_{thom}}{\text{calibration factor}_{thom}} \tag{6.1}$$

and

$$n_0 + \beta^2 n_e = \frac{I_{rayl}}{\text{calibration factor}_{rayl}} \tag{6.2}$$

where I_{thom} and I_{rayl} are the integrated signal of the Thomson respectively the Rayleigh component of a measured spectrum. The calibration factor of the Rayleigh component is 1/143 times the Thomson calibration factor (equation 2.28).
In the past the calibration factors depended strongly on the period of day on which the calibration measurements were performed. Before noon they were approximately 5 % higher and after noon approximately 5 % lower compared with the average calibration factor for one day. The cause of these differences is the laser energy stability and the energy distribution in the laser beam. After revision of the laser the variations in the calibration factors during one day are within 2 %.

As stated in chapter 3, an absolute calibration measurement is a measure of the apparatus profile. This apparatus profile is used in the fit procedure described in chapter 4. So, in principle, each scattering measurement has to be accompanied with an absolute calibration measurement. From the practical point of view and from the measured reproducibility of 2 % in the absolute calibrations it is sufficient to perform the absolute calibration once in two hours.

b Scattering experiments

The reproducibility of the scattering measurements is checked for all measurement series performed. Normally one measurement series is done in two or three days. To check the reproducibility a few measurements are repeated on different times and days. Some results are shown in table 6.1.
It appears, not only for the measurements shown in table 6.1, that the electron density n_e and temperature T_e reproduce within their uncertainties. As the neutral density n_0 depends on the level of the vessel stray light, the reproducibility for n_0 is not so good.

Table 6.1 Reproducibility of the measurements

z (mm)	measured on	n_e (10^{19} m^{-3})	n_0 (10^{20} m^{-3})	T_e (K)
28	10–1	2.02 ± 0.10	4.8 ± 1.4	1824 ± 104
	11–1	2.28 ± 0.10	5.9 ± 1.4	1697 ± 75
50	10–1	2.49 ± 0.10	2.5 ± 1.4	3013 ± 125
	11–1	2.53 ± 0.10	5.3 ± 1.4	3150 ± 130
100	11–1			
	12.20 u	3.25 ± 0.14	8.3 ± 1.4	2993 ± 123
	13.50 u	3.15 ± 0.15	6.6 ± 1.4	2803 ± 130

6.5 Position of the fitted Thomson components of the measurements

In figure 6.2 for two conditions the position of the fitted Thomson components of the measurements is depicted versus the axial position. In figure 6.2a the results for the free expanding plasma are shown. In figure 6.2b the same condition as under 6.2a is depicted, now with a magnetic field applied. The picture is a little suggestive as at lower axial positions (4 – 60 mm) more measurements are performed compared to higher axial positions (60 – 500 mm). More measurements performed at higher axial positions would give the same spread in Thomson position as is seen for low axial positions. The spread in the Thomson position is probably a result of laser beam pointing instability and instability in the position of the lenses and mirrors of the detection optics during a day. For the laser beam pointing instability we have 0.5 mrad. With a distance of 1 meter from the center of the plasma jet to the entrance slit of the polychromator this can result in a deviation of the Thomson position of 0.5 mm which corresponds to 20 pixels. As can be seen in figure 6.2 the time integrated behavior is far more better than this maximum deviation of 20 pixels (the measuring time is 1200 s).

(a) (b)

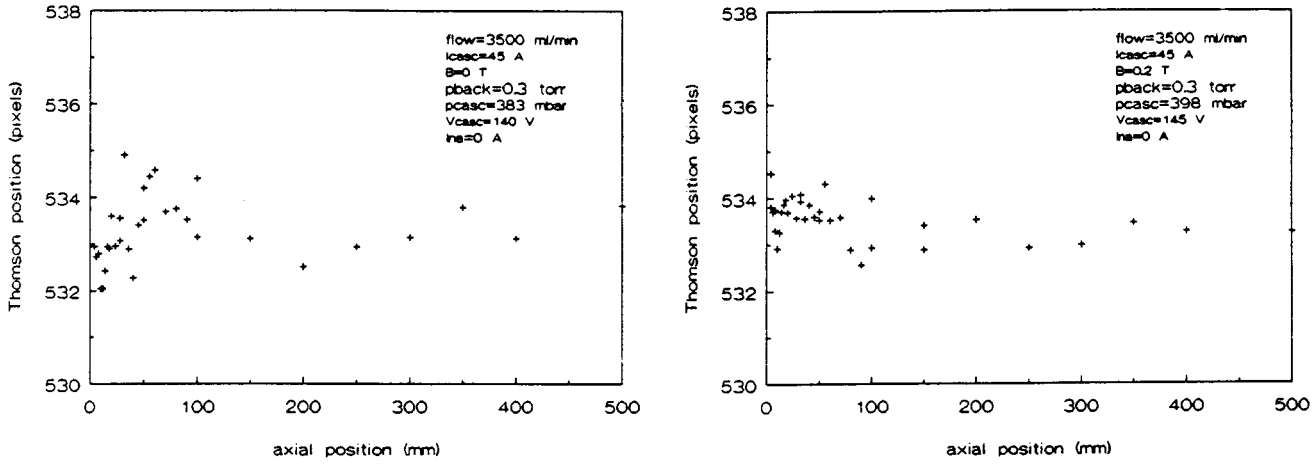

Figure 6.2 *Position of the Thomson components in the measurements: (a) for the free expanding plasma and (b) for the same condition as under (a), now with a magnetic field applied.*

From the data shown in the figure we can determine whether the Thomson position is distributed normally. For a normal distribution 68.3 % of the measured positions has to lie within σ from the mean value; 95.5 % has to lie within 2σ from the mean value. For the free expanding plasma the mean Thomson position is 533.29 pixels with a spread σ of 0.71 pixel. 68.8 % Lies within σ and 96.9 % within 2σ from the mean value.
The numbers for the free expanding plasma with a magnetic field applied are: mean value of 533.54 pixels with σ = 0.44 pixel, 65.7 % lies with in σ and 94.3 % with in 2σ from the mean value. This justifies the conclusion that the average position of the fitted Thomson components of the measurements is normally distributed.

6.6 Distribution of the Chi Square function

The fitting method for our experiments is explained and discussed in chapter 4. In this paragraph we examine the distribution of the Chi Squares of all the fitted measurements performed in this work. See also [26].
The Chi Square is defined as (equation 4.1)

$$\chi^2 = \sum_{i=1}^{N} \left[\frac{y_i - f_i}{\sigma_i} \right]^2 \tag{6.3}$$

where y_i is the measured signal, f_i is the fitted signal, σ_i is the noise in the measured signal and N is the total amount of measured points.
The frequency distribution of the Chi Square values falling in discrete intervals should be the theoretical Chi Square distribution when:

- the error distribution of the measurements is a normal distribution;
- the applied calibrations are correct;
- the used spectral density functions for the Thomson and Rayleigh components of the measurements are correct.

The Chi Square distribution function is given by [27]

$$f(\chi^2) = \frac{(\chi^2)^{(n-1)/2}}{2^{n/2}\Gamma(n/2)} \cdot \exp(-\chi^2/2) \tag{6.4}$$

where n is the degrees of freedom, $f(\chi^2)$ the probability for a Chi Square value of χ^2 and $\Gamma(n/2)$ is the Gamma function. The probability P of a Chi Square with a value between $\chi^2 - \Delta$ and $\chi^2 + \Delta$ is then

$$P(\chi^2) = \int_{\chi^2-\Delta}^{\chi^2+\Delta} f(\chi^2)d\chi^2 \qquad (6.5)$$

In figure 6.3 the distribution of Chi Squares is shown for the experiments and by using equation 6.5. The degrees of freedom n for the two distributions is equal to the amount of measured points minus the amount of parameters of the used model function for one fit. In our case $n = 301 - 7 = 294$. In both cases Δ is taken 20. For the experimental distribution all the Chi Squares of our measurements (with the same degrees of freedom) were taken, in total 124.

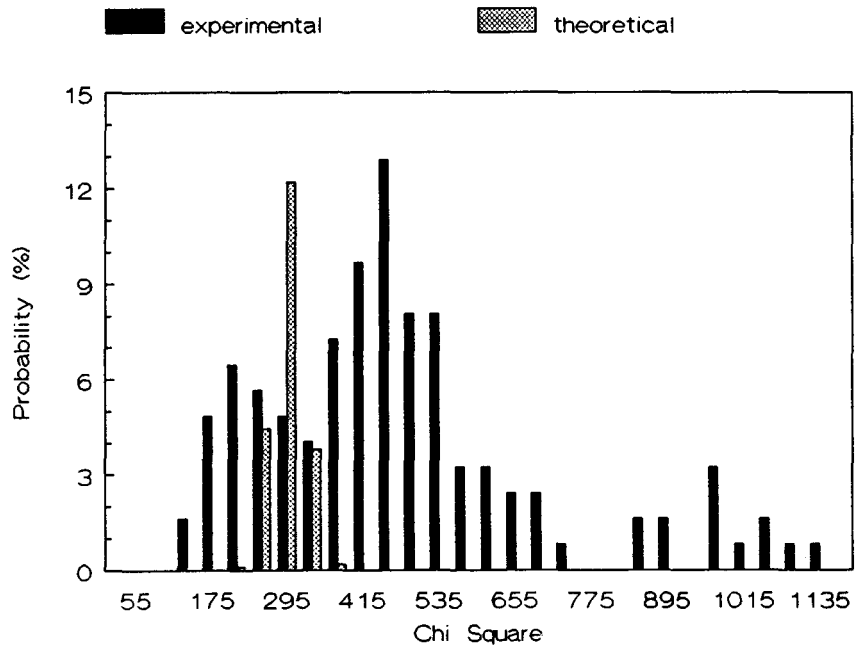

Figure 6.3 Theoretical and experimental distribution of the Chi Squares.

The 124 Chi Squares are collected from measurements done under different conditions. The measurements are performed on a free expanding plasma, with or without a magnetic field applied and with or without a current in the plasma jet. So in total four conditions were measured.

In figure 6.3 we see that there are more large Chi Square values then expected from the theoretical distribution. The peak of the observed Chi Square distribution occurs not at $\chi^2 = 294$, as is expected from the theoretical distribution, but at $\chi^2 \approx 455$. Also more lower Chi Square values are observed than expected.

The observed differences between the theoretical and experimental Chi Square distributions can be explained by:

- relative calibrations. The four measured conditions were spread over half a year. Only before the first and last condition a relative calibration was performed. The first relative calibration was also used for the second and third condition. As a result a systematic deviation is introduced which increases the Chi Square values for the second and third condition.
- stray light. Three conditions were measured with the same amount of vessel stray light. However the last measured condition was done with reduced stray light. This means that the Rayleigh component of the measurements is better determined for the last condition. Of course this reduces the Chi Square values for this condition. This conclusion may explain why more lower Chi Square values are observed than theoretically expected.
- absolute calibration. In the model function of the fit program Rayleigh calibration measurements are used as apparatus profiles. One Rayleigh calibration is used for more than one measurement. This suggests that not always the correct apparatus profile is used in the fit program. This increases the Chi Square values.
- the measurements error may not be normally distributed.
- deviations from a Maxwellian velocity distribution of the electrons. This means that the used spectral density functions are not completely correct. As a consequence the Chi Square values increase.

6.7 Residue investigation

From the fitted measurements the residues are investigated. The residue is defined as measurement minus fit. In figure 6.4 the summation over 31 residues is shown. The residues are calculated from fitted measurements done on an expanding plasma with a magnetic field applied and a current present in the plasma jet. The measurements were performed on different axial positions.

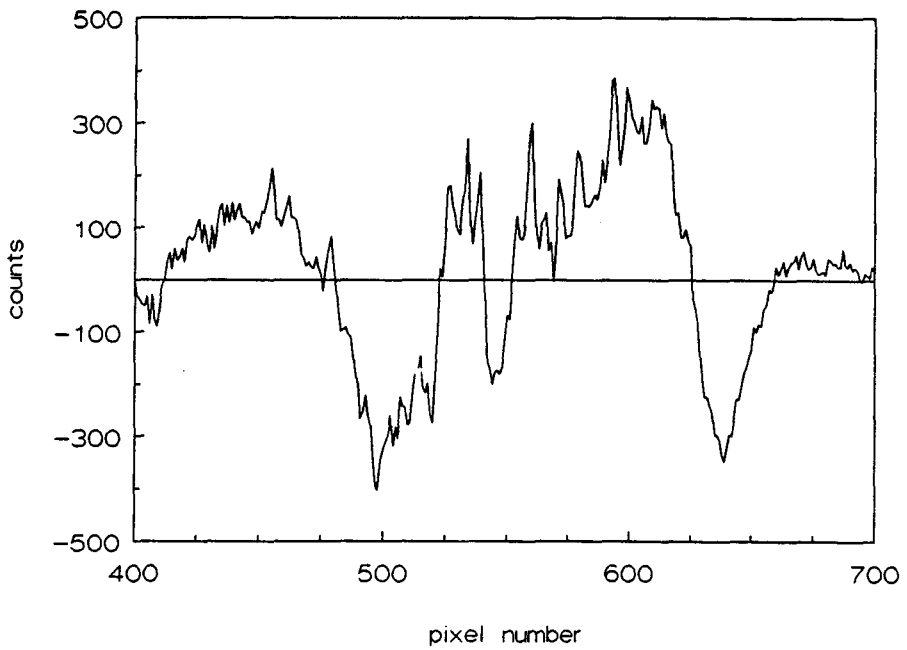

Figure 6.4 *The summed residue of 31 measurements for an expanding plasma with a magnetic field applied and a current present in the plasma jet.*

Clearly the residue is not randomly distributed. We assume that the systematics in the residues can be explained by deviations from a Maxwellian velocity distribution function of the electrons. From the residues a current density $j_\phi = e\Delta n_e v_\phi$ is calculated, where Δn_e denotes the deviation from Maxwell

$$j_\phi \approx e \cdot \sum (p_i - p_{center}) \cdot y_i \cdot \frac{1 \cdot 10^4 \cdot 1 \cdot 10^{19}}{31 \cdot 1000} \qquad (6.6)$$

where p_i is a pixel number, p_{center} is the pixel position of the fitted Thomson component and y_i is the signal (in counts) belonging to p_i. A shift of one pixel corresponds to a rotational velocity of approximately $1 \cdot 10^4$ m/s and 1000 counts correspond approximately to a density of $1 \cdot 10^{19}$ m^{-3}. So equation 6.6 gives the mean azimuthal current density. It should be noted that this calculation implies that the measurements are not performed exactly on the plasma axis. The current density calculated with equation 6.6 is now $j_\phi \approx 7.4 \cdot 10^4$ A/m^2. This result is a factor 10 smaller than the azimuthal current density calculated by [9]. We have to note however that not all the 31 used measurements have the same contribution to the azimuthal current density. This means that the azimuthal current density should not be calculated by dividing the total sum in equation 6.6 by 31 but by a smaller number. As a consequence j_ϕ increases. Second the conditions in [9] were not exactly the same (smaller nozzle, higher current and lower argon gas flow through the cascaded arc and a stronger magnetic field).

6.8 Results of the scattering experiments

Two measured Thomson–Rayleigh spectra are shown in figure 6.5. In figure 6.5a a spectrum measured at 60 mm from the expansion is depicted for the free expanding plasma. The plasma parameters corresponding to the measurement are: $n_e = (3.65 \pm 0.18) \cdot 10^{20}$ m^{-3}, $n_0 = (3.2 \pm 1.4) \cdot 10^{20}$ m^{-3} and $T_e = 3064 \pm 43$ K. The scattering parameter is 0.095 ± 0.004. The influence of an applied magnetic field and a current drawn from the cascaded arc to the end anode is shown in figure 6.5b. Here the position is 90 mm from the expansion. The corresponding plasma parameters are: $n_e = (4.72 \pm 0.20) \cdot 10^{19}$ m^{-3}, $n_0 = (5.2 \pm 1.4) \cdot 10^{20}$ m^{-3} and $T_e = 17112 \pm 467$ K. In this case the scattering parameter is 0.145 ± 0.005.
Both the least mean square fit and the components of the used fit function are given in the figure. The components of the fit function are: a Gaussian corrected for collective effects representing the Thomson component, a scaled apparatus profile representing the Rayleigh component and a linear background. The residue shown is 2 times magnified in figure 6.5a and 5 times magnified in figure 6.5b.

(a) (b)

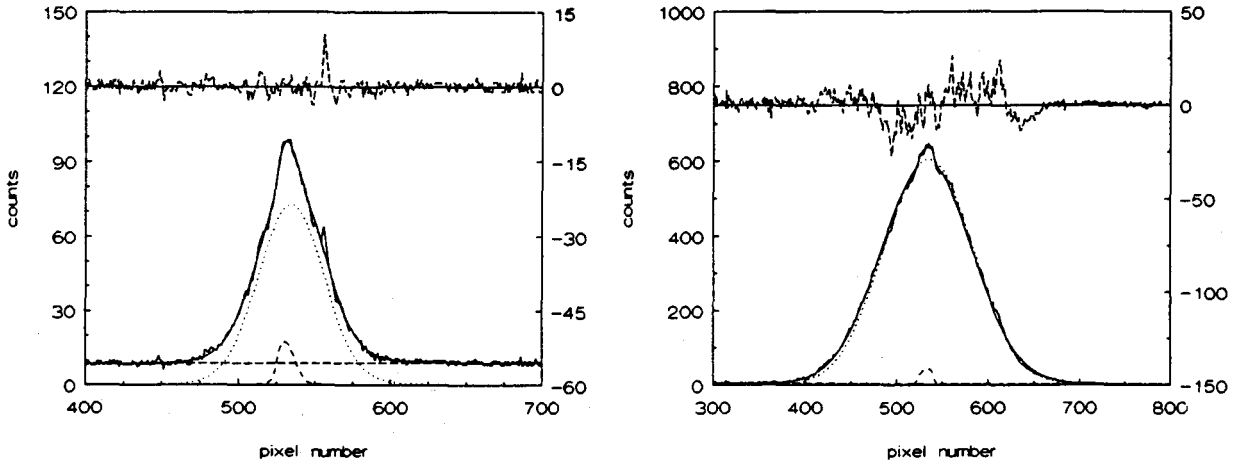

Figure 6.5 *Two measured Thomson–Rayleigh spectra: (a) for the free expanding plasma and (b) for the same condition as under (a), now with a magnetic field applied and a current in the plasma jet.*

The applied magnetic field and current in the plasma jet section in the second measurement explains the large difference in the calculated electron temperatures.
The plasma parameters n_e, n_0 and T_e calculated from the Thomson–Rayleigh measurements are shown in the figures 6.6 – 6.9 for 4 conditions:

- Condition 1: free expanding plasma, shown in figure 6.6.
- Condition 2: the same as condition 1, now with a current in the plasma jet. See figure 6.7.
- Condition 3: the same as condition 1, with a magnetic field applied. See figure 6.8.
- Condition 4: the same as condition 1, with a magnetic field applied and a current in the plasma jet. This condition is shown in figure 6.9.

The exact conditions are as indicated in the figure captions. All measurements are performed on the plasma axis.

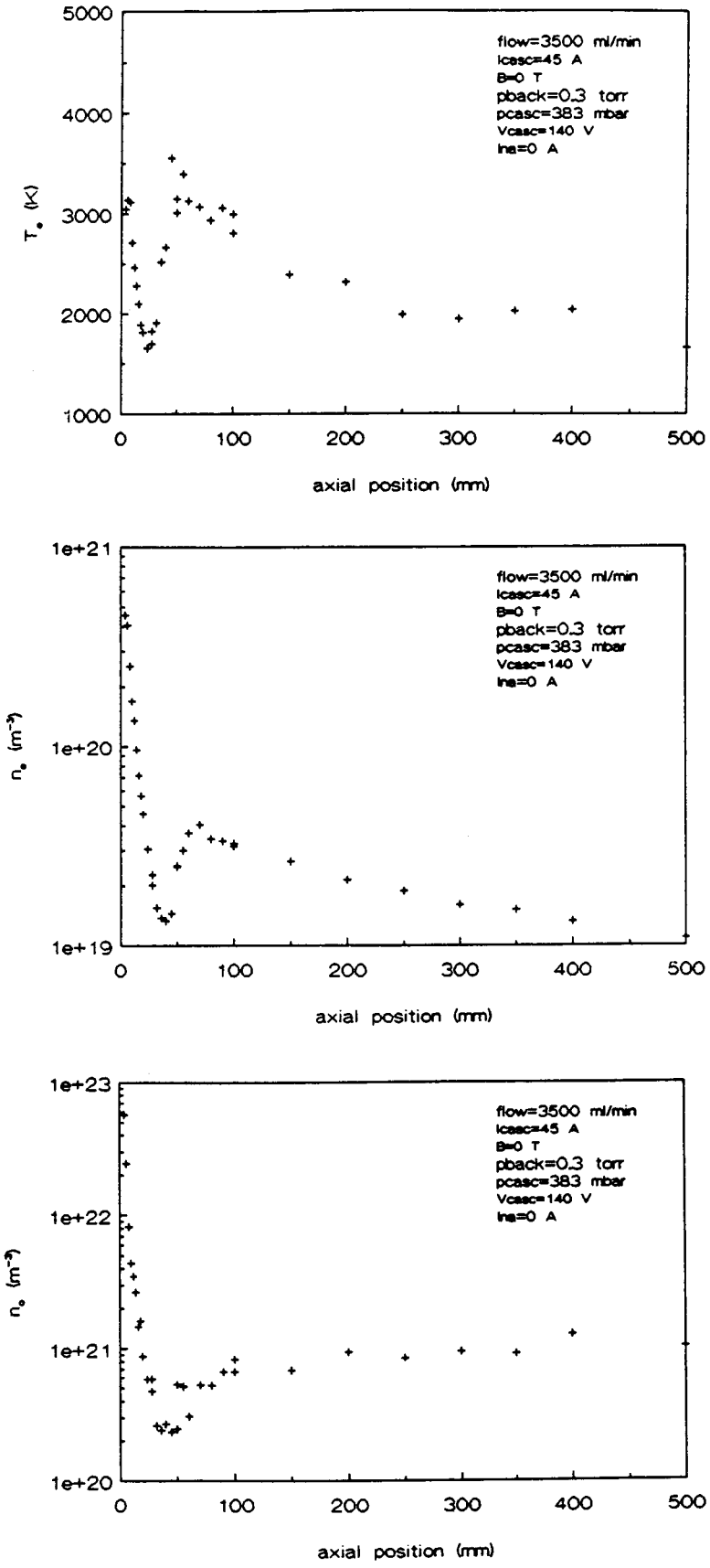

Figure 6.6 *Axial dependence of the plasma parameters for condition 1. Explanation see text.*

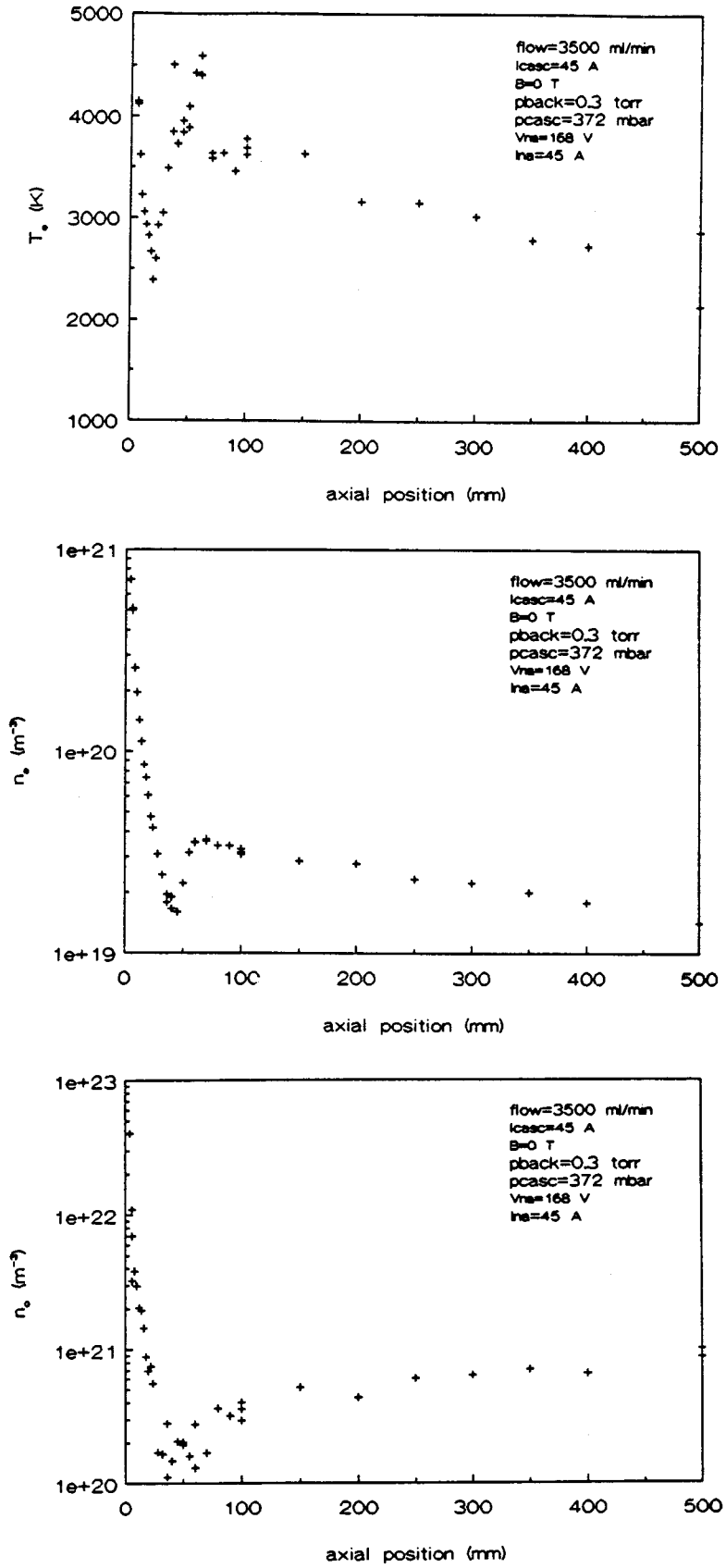

Figure 6.7 *Axial dependence of the plasma parameters for condition 2. Explanation see text.*

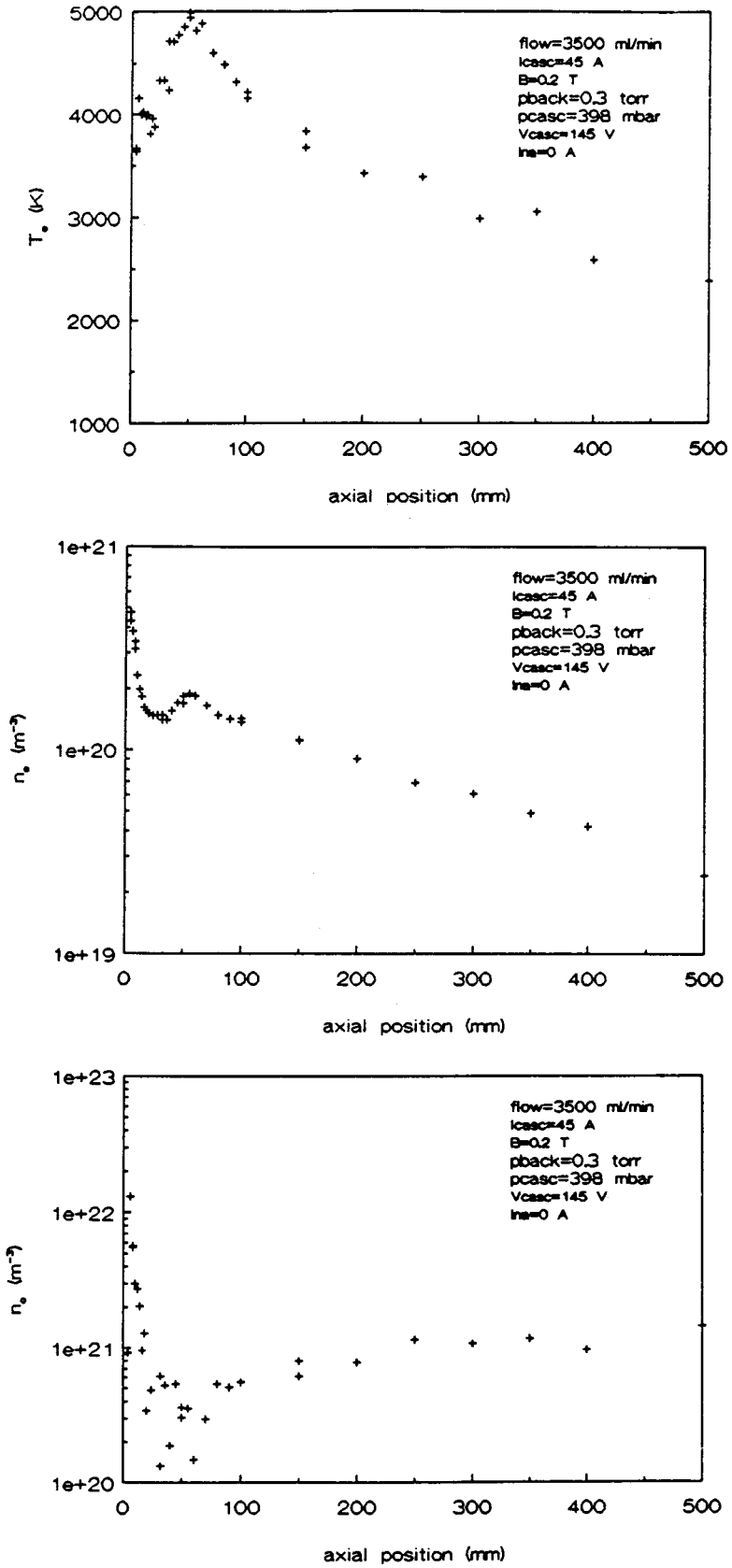

Figure 6.8 *Axial dependence of the plasma parameters for condition 3. Explanation see text.*

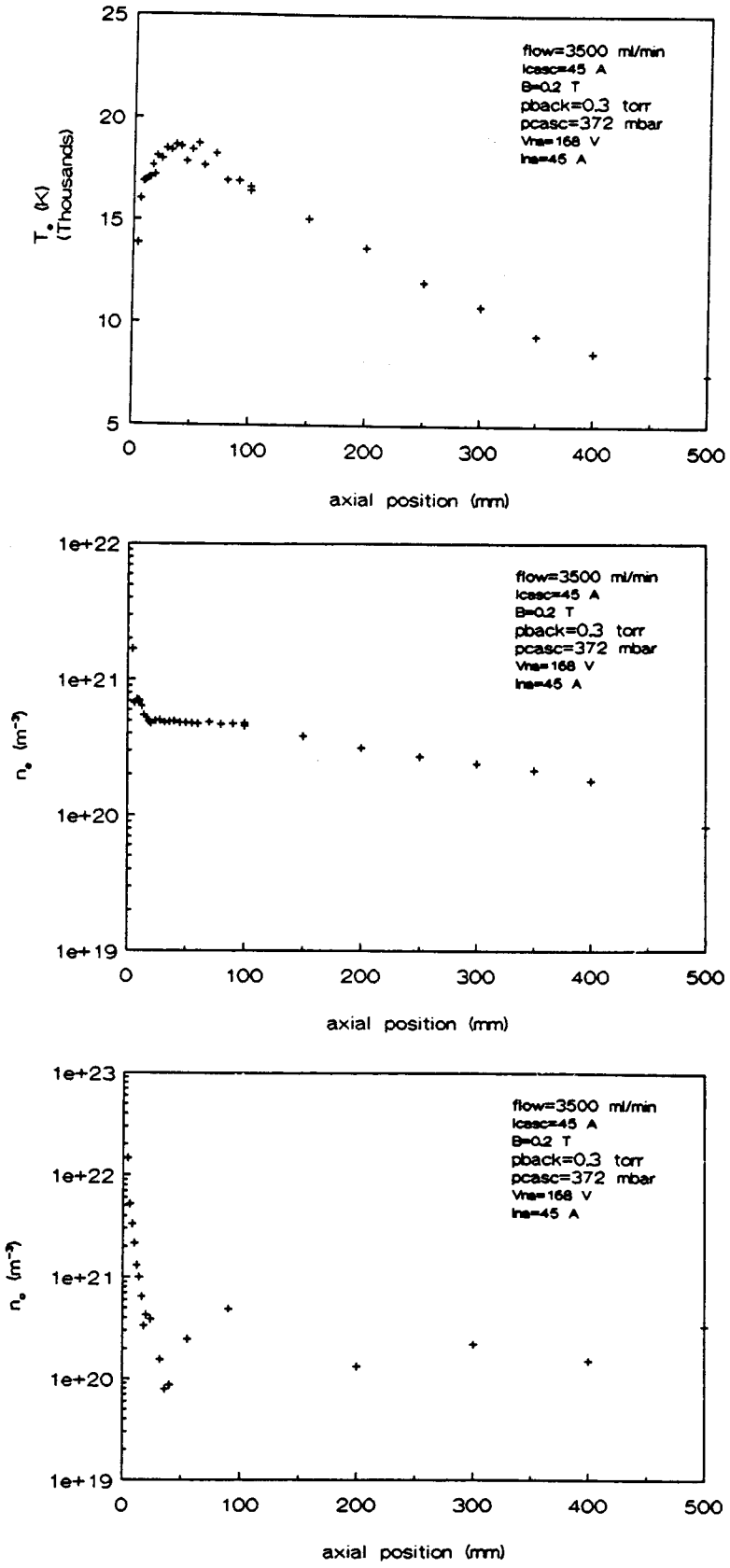

Figure 6.9 *Axial dependence of the plasma parameters for condition 4. Explanation see text.*

From the figures 6.6, 6.7 and 6.9 we see that the measurements show not a normal shock, i.e. the position in the jump of the electron temperature T_e occurs earlier than the jump in the electron density n_e and neutral density n_0. This is an important fact which we explain in chapter 7 by means of current generation in the first part of the expansion.

General structure of the axial dependencies of n_e, n_0 and T_e

Figure 6.6, condition 1:

- The plasma expands in the vacuum vessel at low pressure: n_e, n_0 and T_e decrease due to the expansion.
- In the electron temperature a jump occurs at $z \approx 20$ mm. The electron and neutral densities are still decreasing. The jump can be explained by current generation due to the strong pressure gradient in the first expansion part. This leads to Ohmic heating [6]. See for this point further in this chapter and chapter 7.
- At $z \approx 40$ mm a standing shock wave occurs in the electron and neutral densities.
- Behind the shock subsonic relaxation occurs.

The neutral density is almost the same in the first three conditions (figures 6.6, 6.7 and 6.9). This implies that almost no ionization or recombination take place.

By applying a current in the plasma jet (condition 2) the electron temperature increases. In this case the increase is about 1000 K with a current in the plasma jet of 45 A.This is shown in figure 6.7. The increase in T_e is logical because a current in the plasma jet means Ohmic input. There are two visible differences in n_e and n_0 compared to condition 1. First in the shock is the minimum in n_e higher and the minimum in n_0 lower. This is explained by compressing of the plasma in the shock. Second at high axial positions (300 – 500 mm) is n_0 lower compared to condition 1. See also the analytical expressions for the axial dependence of n_0 given in Appendix A (equations A.3 and A.6). The reason for the small decrease in n_0 is the current in the plasma jet which leads to a higher ionization degree in the plasma (see page 72).

By applying a magnetic field in the plasma jet (condition 3) the plasma is pinched. Now electrons are closer to each other compared to condition 1 and 2 due to the pinching. This increases the electron density and temperature. With a current in the plasma jet (condition 4) this effect is even larger.

From the figure and the analytical expressions given in Appendix A (equations A.3, A.6, A.9 and A.12) we see that for condition 4 the neutral density decreases in the expansion region faster than for the other conditions. In this region the neutral density decreases as a consequence of expansion plus ionization.

The pinching is expressed by the Hall parameter which is equal to $\omega_e \tau_{ee}$, with the cyclotron frequency $\omega_e = eB_z/m_e$ and τ_{ee} the electron – electron collision time ($\tau_{ee} \approx \tau_{ei}$, equation 5.17). This leads to a condition for magnetization of the electrons in the plasma:

$$(\omega_e \tau_{ee})^{-1} = \frac{\rho_e}{\lambda_{ee}} = \frac{\ln\Lambda_c}{9.69 \cdot 10^{15}} \cdot \frac{n_e}{T_e^{3/2}} < 1 \qquad (6.7)$$

where ρ_e is the electron cyclotron radius, λ_{ee} is the electron free path and $\ln\Lambda_c$ the Coulomb logarithm. Under the influence of a magnetic field the electrons cover spiral trajectories. When $\rho_e < \lambda_{ee}$ the electrons cover more spirals between two collisions and the electrons are magnetic confined. In this case we speak of pinching. In figure 6.10 $(\omega_e \tau_{ee})^{-1}$ is depicted as function of the axial position for condition 3 and condition 4. The applied magnetic field is 0.2 T. From figure 6.10 the conclusion is justified that the strength of the applied magnetic field is large enough to pinch the plasma.

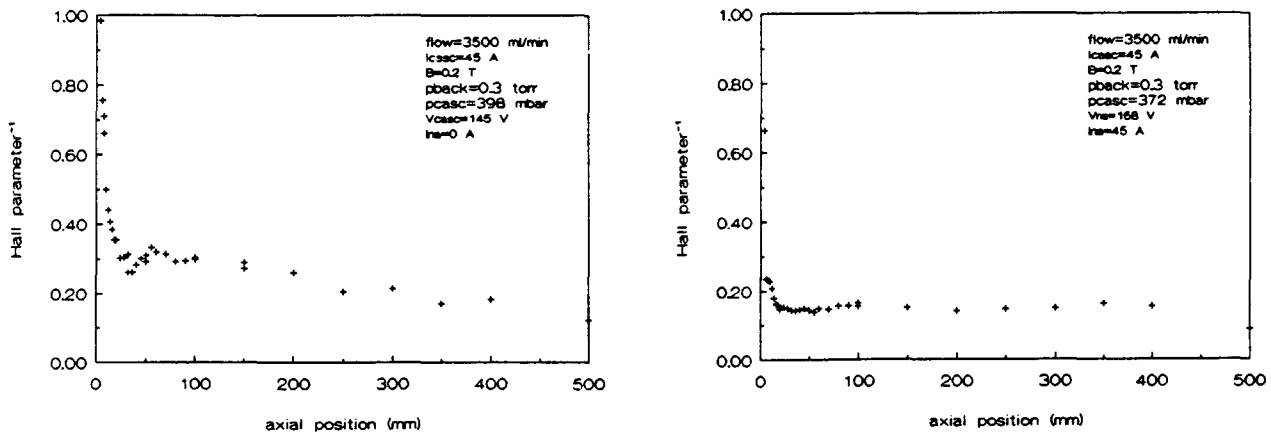

Figure 6.10 *Axial dependence of the inverse Hall parameter; (a) for condition 3 and (b) for condition 4.*

A measure of the ionization in the plasma is given by the ionization degree, which is defined as

$$\alpha = \frac{n_e}{n_e + n_0} \tag{6.8}$$

In figure 6.11 the ionization degree for the 4 conditions is shown.
From the figure it can be seen that the ionization degree increases in the shock, due to the pinching of the plasma in the shock.
Also is seen that the ionization degree increases when a current is present in the plasma jet. When a magnetic field is applied the ionization degree increases further, as expected.
The overpopulation factor of the ground state is

$$b_1 = \frac{n_1}{n_{1s}} \tag{6.9}$$

where n_1 ($= n_0$) is the density of the ground state and the Saha density n_{1s} is given by the Saha equation [22]:

$$n_{1s} = \frac{g_1}{g_e g_i} \cdot \left[\frac{h^2}{2\pi m_e k_b}\right]^{3/2} \cdot \frac{n_e n_i}{T_e^{3/2}} \cdot \exp\left[\frac{E^{1+}}{k_b T_e}\right] \tag{6.10}$$

where $n_i = n_e$ (quasi neutrality) and the statistical weights of the electrons ions and the ground state are $g_e = 2$, $g_i = 6$ respectively $g_1 = 1$.The ionization energy $E^{1+} = 2.524 \cdot 10^{-18}$ J.
The overpopulation factor is shown in figure 6.12. From this figure we see that the ground state is under populated ($b_1 < 1$) for conditions 1, 2 and 3. Only condition 4 shows an overpopulation of the ground state ($b_1 > 1$). This means that condition 1, 2 and 3 show a recombining plasma and condition 4 shows an ionizing plasma.

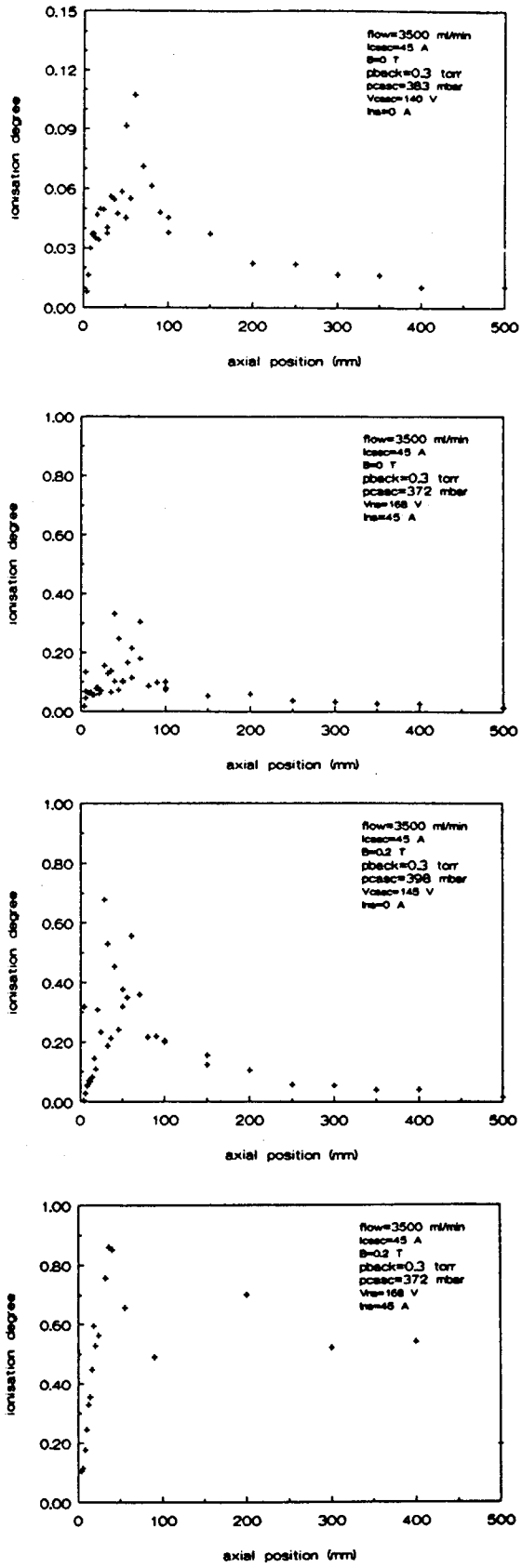

Figure 6.11 Ionization degree for the 4 conditions.

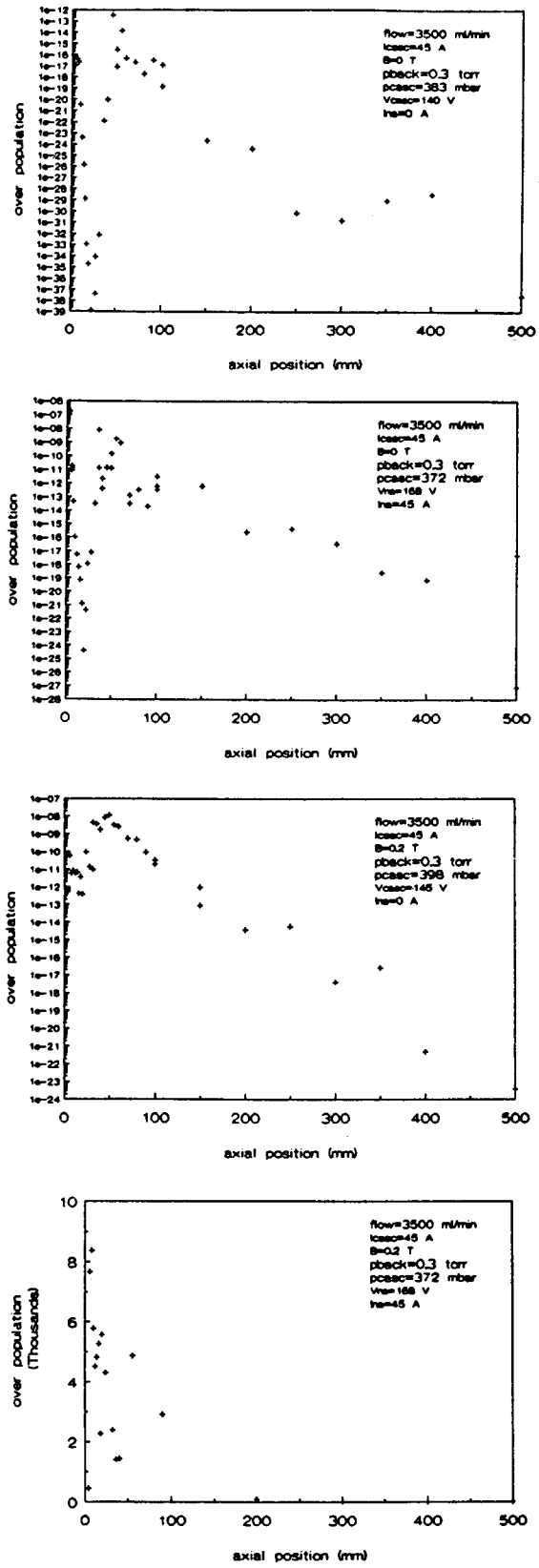

Figure 6.12 Over population factor for the 4 conditions.

In chapter 5 the equations of the free paths for momentum and energy exchange between the electrons, ions and neutrals were given (equations 5.14 – 5.21). For condition 1 at the beginning of the shock ($z \approx 40$ mm) with $n_e = 1.3 \cdot 10^{19}$ m^{-3}, $T_e = 2600$ K, $\ln\Lambda_c = 6.12$, $n_o = 2.0 \cdot 10^{20}$ m^{-3} and $T_i \approx 2300$ K equations 5.14 – 5.16 become:

$$\begin{aligned} \lambda_{ei} &\approx 1.6 \cdot 10^{-4} \text{ m} \\ \lambda_{ii} &\approx 1.2 \cdot 10^{-4} \text{ m} \\ \lambda_{io} &\approx 1.0 \cdot 10^{-2} \text{ m} \end{aligned} \tag{6.11}$$

So the following order is valid in the plasma:

$$\lambda_{ei} \approx \lambda_{ii} \ll \lambda_{io} \tag{6.12}$$

This means that the electron – ion and ion – ion momentum exchange is very fast and takes place on a scale of 0.1 mm. The ion – neutral exchange is slower and takes place on a scale of 10 mm. So the ion -- neutral exchange determines the thickness of the shock. As λ_{io} only depends on T_h and n_o (equations 5.16 and 5.19) and because the neutral density is approximately the same for conditions 1, 2 and 3 the thickness of the shock remains constant for conditions 1, 2 and 3 (in condition 4 no shock occurs). This is also seen in figures 6.6, 6.7 and 6.8.

The mean free path for energy exchange between electrons and ions is given by equation 5.20. For the values of n_e and T_e given above this becomes

$$\lambda_{ei}^{\epsilon} \approx 5.8 \text{ m} \tag{6.13}$$

This means that on a plasma scale of 0.5 m there is not much energy exchange between the electrons and ions. The consequence is that the electron and heavy particle temperatures remain different or are decoupled after the shock if they are different in front of the shock. Here we suggested that $T_i \approx T_o \approx T_h$. This is a fair suggestion because the mean free path for energy exchange between ions and neutrals is the same as for momentum exchange (equation 5.21), i.e. in the order of 10 mm:

$$\lambda_{io}^{\epsilon} \approx 1.0 \cdot 10^{-2} \text{ m} \tag{6.14}$$

This means that the energy exchange between the ions and neutrals is very fast.

The magnitude of the jumps in the plasma parameters is determined by the Rankine–Hugoniot relations. These equations were given in chapter 5 (equations 5.9 – 5.12) under the assumptions that $w_i = w_0 = w_h$ and $T_i \approx T_0 \approx T_h$ (no magnetic field applied).
In table 6.2 the Mach number M_1 and the jumps in w_h, p and T_h calculated with the Rankine–Hugoniot relations are listed for condition 1 and 2. Point 1 is at z = 40 mm and point 2 is at z = 60 mm.

Table 6.2 Results of the Rankine–Hugoniot relations for condition 1 and 2.

	Condition 1	Condition 2
ρ_2/ρ_1	2.0	1.3
M_1	1.7	1.2
w_{h2}/w_{h1}	0.5	0.8
p_2/p_1	3.4	1.6
T_2/T_1	1.7	1.2

From this table we see that the jump in the plasma parameters for condition 1 is larger then for condition 2. We return to this subject in chapter 7.

The position of the shock in the electron and neutral densities can be calculated with equation 5.22. In our 4 measured conditions the background pressure $p_\infty = 40$ Pa and the effective nozzle diameter $d^* = 4.0$ mm. The pressure at the nozzle exit is calculated from the pressure balance. Here it is assumed that the temperature of the electrons equals the temperature of the ions and neutrals and that $n_i = n_e$ (quasi neutrality).
Values of the electron temperature, electron density and neutral density at the nozzle exit are obtained from an analytical expression of the profile shown in figure 6.6. The analytical expressions are given in Appendix A (equations A.1 – A.3). The pressure balance then reads

$$p_0 = (2n_e + n_0)\cdot k_b T_e \qquad (6.15)$$

The pressure p_0 can also be calculated from the sonic flow at the nozzle exit.
For condition 1, the free expanding plasma, $p_0 \approx 1.1 \cdot 10^4$ Pa. According to this pressure the location of the Mach–disk is at $x_M \approx 43$ mm. This result is in good agreement with the location determined from the experiments: 40 mm. The little difference between the calculated and observed location is explained by the large gradients in the temperature and density profiles close to the nozzle. Therefore the extrapolated values to the position of the nozzle exit are rough estimations.

We discussed already that for a normal shock the jumps in T_e and the jump in the densities n_e and n_0 occur at the same position. However in our measurements we see a significant difference in the position of the jump in T_e compared to the jump in n_e and n_0. This is also measured by ref. [6]. The explanation according to ref. [6] is current generation due to the strong pressure gradient in the first expansion zone. This strong pressure gradient is illustrated when we compare the pressure at the nozzle exit with the pressure at the beginning of the shock. We saw already that at $z = 0$ mm $p \approx 11400$ Pa. At the beginning of the shock ($z \approx 40$ mm) $p \approx 7$ Pa where the pressure is calculated using the pressure balance $p = \Sigma n_x k_b T_x$ with the subscript x for electrons, ions and neutrals and $n_e =$. Thus in the first expansion zone ($0 - 40$ mm) we see a decrease in the pressure of almost three orders.
In the next chapter we try to calculate the current density from the electron energy balance to check the explanation given by ref. [6].

7 Calculation of the current density

7.1 Introduction

In chapter 6 we saw that the position of the jump in the electron temperature occurs closer to the nozzle exit than the jump in the electron and neutral density. As we already discussed in chapter 1 and 6, the literature does not give an adequate answer to this phenomenon. A possible explanation of the different positions in the T_e jump and the jump in the electron and neutral densities is given by [6]: current generation due to the strong pressure gradient in the first section of the expansion. The generated current then heats the electrons through Ohmic dissipation.
The purpose of this chapter is to check the explanation for the difference in positions of the jumps proposed above for one measured condition. We do this for the free expanding plasma by calculating the current density on the axis of the plasma jet. In all cases the plasma is considered to be stationary.
The current density is given by

$$\mathbf{j} = -\,en_e(\mathbf{w}_e - \mathbf{w}_i) \tag{7.1}$$

where $\mathbf{j}$ is the current density and $\mathbf{w}_{e,h}$ is the drift velocity of the electrons respectively the heavy particles (neutral atoms and ions).
From equation 7.1 we see that $\mathbf{w}_{e,i}$ has to be calculated first to determine $\mathbf{j}$. In paragraph 7.2 a model is presented to calculate $\mathbf{j}$ with the help of a simplified electron energy balance. In the electron energy balance two other unknown plasma parameters are present, namely the heavy particle velocity and the heavy particle temperature. A possible way to calculate these two parameters is shortly considered in paragraph 7.3.
The following assumptions are made (see also chapter 5):

- the energy coupling between the ions and neutrals is strong: $T_i = T_o = T_h$;
- a large friction between the ions and neutrals exists: $\mathbf{w}_i = \mathbf{w}_o = \mathbf{w}_h$.

7.2 The Electron Energy Balance

The energy balance for the electrons reads for a stationary plasma [28]

$$\nabla\cdot\left[\frac{3}{2}n_e k_b T_e \mathbf{w}_e\right] + n_e k_b T_e \nabla\cdot\mathbf{w}_e + \boldsymbol{\Pi}_e:\nabla\mathbf{w}_e + \nabla\cdot\mathbf{q}_e = Q^e \qquad (7.2)$$

where n_e, $\mathbf{w}_e$ and T_e are the density, velocity and temperature of the electrons. k_b Is the Boltzmann constant, $\boldsymbol{\Pi}_e$ is the viscosity tensor, $\mathbf{q}_e$ is the thermal heat flux of the electrons and Q^e is the source term for the electrons. $\boldsymbol{\Pi}_e:\nabla\mathbf{w}_e$ represents the viscous dissipation, $\nabla\cdot\mathbf{q}_e$ the heat conduction and Q^e all other energy supplied to the electrons by collisions with other particles. Q^e consists of several terms, in general:

$$Q^e = Q_{eh}{}^e + Q_{3d}{}^e + Q_{fb}{}^e + Q_{ff}{}^e + Q_{ohm}{}^e \qquad (7.3)$$

where:

$Q_{eh}{}^e$ represents the elastic energy exchange with the ions and the neutrals;
$Q_{3d}{}^e$ is the energy loss due to collisional excitation/deexcitation and ionization/three–particle recombination (energy loss term);
$Q_{fb}{}^e$ represents the radiative recombination (energy loss term);
$Q_{ff}{}^e$ represents the brehmstrahlung (energy loss term);
$Q_{ohm}{}^e$ represents the Ohmic heating of the electrons (energy gain term).

The calculation of all source terms is shown in Appendix B. Of these terms $Q_{3d}{}^e$, $Q_{fb}{}^e$ and $Q_{ff}{}^e$ are small compared to $Q_{eh}{}^e$ and $Q_{ohm}{}^e$. So the most important terms are [28], [29]:

$$Q_{eh}{}^e = -3\cdot\frac{m_e}{m_h}n_e\frac{1}{\tau_{eh}}k_b(T_e - T_h) \approx Q_{ei}{}^e =$$

$$= -2.07\cdot10^{-33}\ln\Lambda_c\frac{n_e{}^2}{T_e{}^{3/2}}(T_e - T_h) \qquad (7.4)$$

where $\frac{1}{\tau_{eh}} = \frac{1}{\tau_{ei}} + \frac{1}{\tau_{eo}}$ with τ_{ei} from equation 5.17 and $\tau_{eo} = 5.7\cdot10^{14}/n_o T_e{}^{3/10}$ according to [22].

$$Q_{ohm}{}^{e} = \eta \mathbf{j}\cdot\mathbf{j} = 3.31\cdot 10^{-36} \ln\Lambda_c \frac{n_e{}^2}{T_e{}^{3/2}} (\mathbf{w}_e - \mathbf{w}_i)^2 \tag{7.5}$$

where $\eta = \frac{m_e}{n_e e^2 \tau_{ei}}$ is the resistivity of the plasma.
In equation 7.2 now all the terms are known, so in principle the electron velocity on the plasma axis, w_{ez} can be calculated.
In our model, consisting of the electron energy balance we suppose that:

- only the Ohmic heating is important. This is reasonable when $10^{-3}\cdot(\mathbf{w}_e - \mathbf{w}_i)^2 \gg (T_e - T_h)$.
- the heat conduction and the viscous dissipation can be neglected;
- $\mathbf{w}_e \gg \mathbf{w}_i$, which means that the current is carried by the electrons: $\mathbf{j} \approx -en_e\mathbf{w}_e$.

The mass balance for the electrons reads with the assumption that recombination is of no account:

$$\nabla\cdot(n_e\mathbf{w}_e) = 0 \rightarrow \nabla\cdot\mathbf{w}_e = -\frac{\mathbf{w}_e\cdot\nabla n_e}{n_e} \tag{7.6}$$

Substitution of equation 7.5 and 7.6 in equation 7.2 gives an expression for the current density on the plasma axis:

$$j_z = \frac{T_e{}^{3/2}}{128.83\cdot\ln\Lambda_c}\left[\frac{k_b T_e}{e n_e}\frac{\partial n_e}{\partial z} - \frac{3k_b}{2e}\frac{\partial T_e}{\partial z}\right] \tag{7.7}$$

We do not use Ohms law to calculate j_z because then we need to know the value of the electric field. When j_z is known From the electron momentum balance the generated electric field can be calculated [9]:

$$E_z = -\frac{1}{en_e}\frac{\partial p_e}{\partial z} + \eta j_z \tag{7.8}$$

In the right hand side of equation 7.7 all the variables are known. The derivatives of n_e and T_e with respect to z are calculated from the analytical expressions for n_e and T_e for the free expanding plasma given in Appendix A (condition 1). The current density j_z calculated with equation 7.7 is shown in figure 7.1. The generated electric field is shown in figure 7.2.

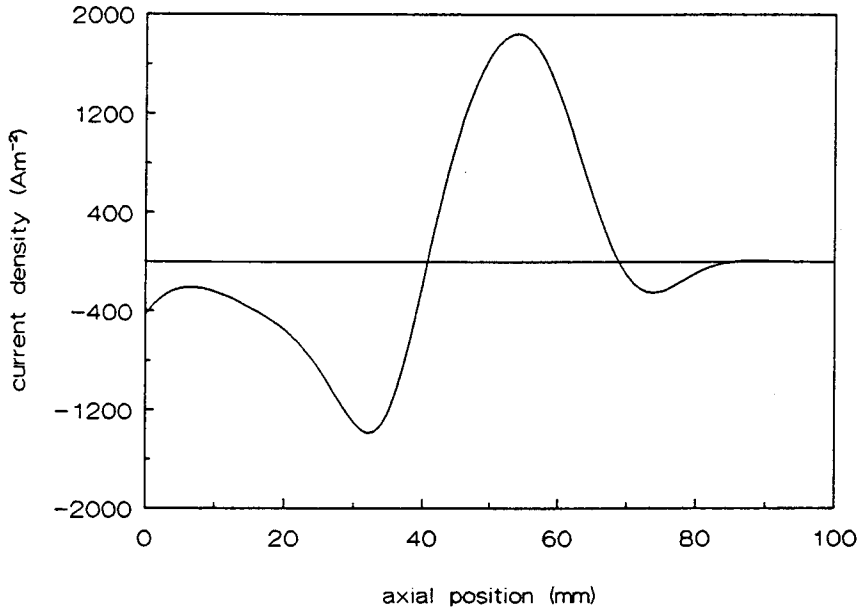

Figure 7.1 *The axial current density for a free expanding plasma, calculated with the electron energy balance.*

Close to the nozzle exit the current density should be zero. The current density at z = 0 mm visible in figure 7.1 is explained from the form of the analytical expressions for T_e and n_e given in Appendix A. The current density is generated by the exponents and the decay of the exponents covering the first expansion region. The decay in the exponents does not take into account that at z = 0 mm the gradients in T_e and n_e should be smaller than calculated from equations (A.1) and (A.3) which would lead to a negligible current density. The dashed curve in figure 7.1 represents the current density close to the nozzle exit the way it should be.
In the picture we see current densities varying from $-1.5 \cdot 10^3$ A/m^2 to $2.0 \cdot 10^3$ A/m^2.
The positive and negative current densities can be explained by convective cells. This is demonstrated in figure 7.3.

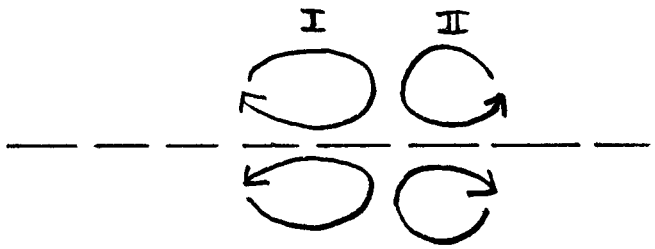

Figure 7.2 Convective cells round about the plasma axis.

The convective cells denoted with I account for the positive current density in figure 7.1. The convective cells denoted with II represent the negative current density in figure 7.1. From $j_z = -en_e w_{ez}$ electron velocities of 10^1 to 10^3 m/s are calculated. Clearly these are too small to neglect w_{iz}.
We have to draw the following conclusion: the shape of the current density calculated with the simplified electron energy balance looks reasonable. Because the calculated electron velocities are small, however, it is not sufficient to assume that $\mathbf{w}_e \gg \mathbf{w}_h$. This means that also the heavy particle velocity has to be determined to calculate the current density. This implies also that the heavy particle temperature has to be calculated.
In the next paragraph we discuss a possible method to calculate $\mathbf{w}_h$ and T_h.

7.3 A method to determine the current density more accurate

In chapter 5 the conservation equations when crossing the shock, the Rankine–Hugoniot relations (equation 5.9 – 5.12) were given. We saw that the jump in the plasma parameters when crossing the shock is completely determined by the Mach number M_1 before the shock.
From equation 5.9 M_1 can be calculated because ρ is known in front of and behind the shock. Then w_{h1} can be calculated from $M_1 = w_{h1}/c_1$ and w_{h2} from equation 5.10.
The heavy particle temperature behind the shock is determined from the pressure balance, with the pressure equal to the background pressure:

$$p = \sum n_x k_b T_x = p_{background} = 40 \text{ Pa} \tag{7.9}$$

where the subscript x denotes electrons, ions or neutrals. Then with equation 5.12 the heavy particle temperature before the shock can be calculated.
The heavy particle temperature on different axial positions from z= 0 mm to the beginning of the shock can be calculated from the relation for adiabatic expansion:

$$\frac{p}{\rho^\gamma} = \text{constant} \tag{7.10}$$

where $\gamma = 5/3$. Notice that this equation also follows from the electron energy balance (equation 7.2) with Q^e negligible on the first zone of the expansion (0 – 20 mm) and the assumption of no viscous dissipation and heat conduction.
The heavy particle velocity is calculated from [17]:

$$w_h^2 = c_0^2 + \frac{\gamma}{2\gamma-1}.\frac{p_0}{\rho_0}.\left[1 - \left[\frac{\rho}{\rho_0}\right]^{\gamma-1}\right] \tag{7.11}$$

where c_0 is the velocity of sound (from equation 5.8) and p_0 and ρ_0 the pressure respectively mass density on $z = 0$. Equation 7.10 is valid only for adiabatic expansion, i.e. when equation 7.10 is valid.
The heavy particle velocity before the shock is determined by the total momentum balance. On the plasma axis this reduces to:

$$m_0(n_e + n_0)w_h\frac{\partial w_h}{\partial z} = -\frac{\partial p}{\partial z} \tag{7.12}$$

where $p = \sum n_x k_b T_x$, with the subscript x for electrons, ions or neutrals. Equation 7.11 gives for the heavy particle velocity

$$w_h^2(z_2) = w_h^2(z_1) - \int_{z_1}^{z_2} \frac{2}{\rho} \frac{\partial p}{\partial z} dz \tag{7.13}$$

Conclusion: the combination of the electron energy balance (equation 7.2), the equations for adiabatic expansion (equations 7.10 and 7.11), the total momentum balance (equation 7.13) and the Rankine–Hugoniot relations gives a means to calculate $\mathbf{w}_h$, T_h, $\mathbf{w}_e$ and from these values $\mathbf{j}$ on the axis of the plasma.

8 Conclusions and suggestions

A fit program has been developed to determine the electron density n_e, electron temperature T_e and neutral density n_0 more accurate than in the past. The following conclusions are drawn

- By means of convolution procedures the accuracy in the calculated plasma parameters is increased.

- Corrections for collective effects are introduced. It is proved that even for small scattering parameters ($\alpha \simeq 0.2$) correction is necessary.

- From the conclusions given above the best model function used in the fit program consists of a linear background plus a Gaussian, if necessary corrected for collective effects, convoluted with a measured apparatus profile plus a scaled apparatus profile. The first component reflects the background of a scattering measurement (not the same for all measurements), the second component represents the Thomson component of a scattering measurement and the third component represents the Rayleigh component of a scattering measurement. The reached accuracies are for n_e $1-4$ %, for T_e $2-4$ % and for n_0 $10-20$ %.

Measurements on shock wave phenomena are performed. From the measurements we can draw the following conclusions:

- The position of the jump in the electron temperature differs from the position of the jumps in the electron and neutral densities in contrast with a normal shock.

- An explanation is given by current generation due to the strong pressure gradient in the first part of the expansion. The current density is calculated using the electron energy balance. The calculated current densities are in the order of $-1.5 \cdot 10^3$ A/m^2 to $2.0 \cdot 10^3$ A/m^2 and can be explained by convective cells around the plasma axis.

- The electron velocities calculated from the current density are too small to neglect the heavy particle velocities in the electron energy balance. A method is given to calculate correctly the heavy particle velocity and temperature and the electron velocity on the axis of the plasma. From these values the current density can then be calculated.

Suggestions:

- We gave a method to calculate the current density more correctly than was done in this work. It is interesting to use this method in practice and deepen it.

- The possibilities are present in the cascaded arc set up to use Fabry–Perot interferometry. This is a diagnostic which measures the neutral and ion temperatures and the axial and azimuthal ion velocities. Together with Thomson–Rayleigh scattering this means that all the plasma parameters necessary for the calculation of the current density are experimentally determined.

- Together with Fabry–Perot interferometry Thomson–Rayleigh scattering measurements give the possibility to compare the experimental determined current density with the current density calculated with the model discussed above.

- The accuracy in the neutral density strongly depends on the vessel stray light. Therefore reduction of the vessel stray light is necessary to reach a better accuracy in the neutral density. At the moment this is done by using anti–reflection coated windows and a longer tube for the laser dump. The level of the vessel stray light decreases to approximately 200 counts, which means an improvement of a factor 4.

References

[1] Z. Qing, Internal report VDF/NT 90–19, Eindhoven University of Technology, 1990.

[2] M. Huang, G.M. Hieftje, A new procedure for determination of electron temperatures and electron concentrations by Thomson scattering from analytical plasmas, Spectrochimica Acta. vol.44B, no.3, pp. 291–305, 1989.

[3] M. Huang, P.Y. Yang, D.S. Hanselman, C.A. Monnig, G.M. Hieftje, Verification of a Maxwellian electron–energy distribution in the ICP, Spectrochimica Acta. vol.45B, no.4/5, pp. 511–520, 1990.

[4] G.M.W. Kroesen, Plasma Deposition: Investigations on a new approach, Ph. D. Thesis, Eindhoven University of Technology 1988.

[5] F. Siemsen, Bericht der Kernforschungsanlage Jülich Nr.926, 1973.

[6] D.H. McNeill, Electron heating in collisional shocks, Phys. Fluids, vol.18, no.1, january 1975, pp. 44–50.

[7] J. Sheffield, Plasma Scattering of Electromagnetic Radiation, Academic Press, New York 1975.

[8] P. Jauernik, Thomsonstreulichtmessung der raumlichen verteilung der temperatur und dichte eines niederdrucklichtbogenplasmas mit hilfe eines vielkanalspektrometers, Ph. D. Thesis, University of Dusseldorf 1986

[9] H. Gielen, On the electric and magnetic field generation in expanding plasmas, Ph.D. thesis, Eindhoven University of Technology 1989.

[10] Spectra Physics, Specifications and manual guide book Nd:YAG laser.

[11] M.C.M. van de Sanden, Internal report, Eindhoven University of Technology 1988.

[12] J.J. Bleize, C.J. Timmermans, Internal report VDF/NT 88–16, Eindhoven University of Technology 1988.

[13] H.J. Kunze, The laser as a tool for plasma diagnostics, in Plasma Diagnostics edited by W.Lochte–Holtgreven, North–Holland Publishing Company, Amsterdam 1968, pp. 550–616.

[14] W.H. Press, B.P. Flannery, S.A. Teukolsky, W.T. Vetterling, Numerical Recipes in Pascal, Cambridge University Press, New York 1989.

[15] G.M. Janssen, User guide of the fit program, Internal report, Eindhoven University of Technology 1990.

[16] P.A. Burm, Het kleinste kwadraten procedure pakket, Internal report VDF/CO 84–14, Eindhoven University of Technology 1984.

[17] L.D. Landau, E.M. Lifshitz, Course of Theoretical Physics, vol.6, 2nd edition, Pergamon Press 1987.

[18] J.A. Owczarek, Fundamentals of Gas Dynamics, International Textbook Company, Scranton 1964.

[19] Y.B. Zel'dovich, Y.P. Raizer, Physics of Shock Waves and High–Temperature Hydrodynamic Phenomena, vol.1, Academic Press, New York 1966.

[20] R. van Dongen, Gasdynamica I, Eindhoven University of Technology 1988.

[21] K.C. Hsu, Ph. D. Thesis, University of Minnesota, 1982.

[22] B. van der Sijde, Inleiding Plasmafysica, Eindhoven University of Technology 1989.

[23] B.F.M. Pots, Turbulence and transport in a magnetized Argon plasma, Ph. D. Thesis, Eindhoven University of Technology 1979.

[24] H. Ashkenas, F.S. Sherman in Rarified Gas dynamics, edited by J.H. de Leeuw, vol.2, p.84, Academic, New York 1966,

[25] W.S. Young, Derivation of the free–jet Mach–disk location using the entropy–balance principle, Phys. of Fluids, vol.18, no.11, pp. 1421–1425, november 1975.

[26] H. Fajemirokun, C. Gowers, P. Nielsen, H. Salzmann, K. Hirsch, A new method for estimating and identifying systematic error in Thomson scattering diagnostics, Rev. Sci. Instrum. 61 (10), pp. 2849–2851, october 1990.

[27] Standard Mathematical Tables, 17^{th} edition, pp. 577–578, The Chemical Rubber Co. 1969.

[28] S.I. Braginskii, Transport processes in a plasma, in Reviews of plasma physics vol.1, edited by M.A. Leontovich, pp. 205–311, New York 1965.

[29] G.M.W. Kroesen, D.C. Schram, C.J. Timmermans, J.C.M. de Haas, The Energy Balance of a Plasma in Partial Local Thermodynamic Equilibrium, IEEE Transactions on plasma science, vol.18, no.6, pp. 985–991, december 1990.

Appendix A

As stated before Thomson–Rayleigh scattering measurements were performed on 4 conditions:

- condition 1: a free expanding plasma;
- condition 2: the same as condition 1, now with a current in the plasma jet;
- condition 3: the same as condition 1, with a magnetic field applied;
- condition 4: the same as condition 1, now with a magnetic field applied and a current in the plasma jet.

All measurements were performed on the axis of the plasma jet. In this appendix the analytical expressions for n_e, n_0 and T_e derived from the measurements are given.
In these expressions is z the axial position in mm.

Condition 1

$$T_e(z) = 8000\cdot\exp\left[-\frac{z}{11}\right] + 3200\cdot\exp\left[-\frac{z}{700}\right] - 3100\cdot\exp\left[-\left[\frac{z}{35}\right]^4\right] + \\ + 550\cdot\exp\left[-\left[\frac{z-50}{20}\right]^2\right] \qquad (A.1)$$

$$n_e(z) = 9\cdot10^{20}\cdot\exp\left[-\frac{z}{7.3}\right] + 4\cdot10^{19}\cdot\exp\left[-\frac{z}{380}\right] - 4\cdot10^{19}\cdot\exp\left[-\left[\frac{z}{50}\right]^4\right] + \\ + 1\cdot10^{19}\cdot\exp\left[-\left[\frac{z-65}{10}\right]^2\right] \qquad (A.2)$$

$$n_0(z) = 1\cdot10^{23}\cdot\exp\left[-\frac{z}{4.5}\right] + 1.1\cdot10^{21} - 4.4\cdot10^{22}\cdot\frac{150}{z^2+75^2} \qquad (A.3)$$

Condition 2

$$T_e(z) = 6000\cdot\exp\left[-\frac{z}{11}\right] + 4200\cdot\exp\left[-\frac{z}{800}\right] - 3000\cdot\exp\left[-\left[\frac{z}{30}\right]^5\right] + \\ + 450\cdot\exp\left[-\left[\frac{z-55}{20}\right]^2\right] \qquad (A.4)$$

$$n_e(z) = 7\cdot 10^{20}\cdot\exp\left[-\frac{z}{10}\right] + 4\cdot 10^{19}\cdot\exp\left[-\frac{z}{500}\right] - 4.8\cdot 10^{19}\cdot\exp\left[-\left[\frac{z}{50}\right]^5\right] \tag{A.5}$$

$$n_o(z) = 5\cdot 10^{22}\cdot\exp\left[-\frac{z}{4.5}\right] + 9\cdot 10^{20} - 6.8\cdot 10^{22}\cdot\frac{300}{z^2 + 150^2} \tag{A.6}$$

Condition 3

$$T_e(z) = 4000\cdot\exp\left[-\frac{z}{5}\right] + 4700\cdot\exp\left[-\frac{z}{700}\right] - 1100\cdot\exp\left[-\left[\frac{z}{38}\right]^4\right] + \\ + 700\cdot\exp\left[-\frac{(z - 50)^2}{650}\right] \tag{A.7}$$

$$n_e(z) = 8\cdot 10^{20}\cdot\exp\left[-\frac{z}{4.5}\right] + 2\cdot 10^{20}\cdot\exp\left[-\frac{z}{240}\right] - 4.5\cdot 10^{19}\cdot\exp\left[-\left[\frac{z}{50}\right]^4\right] + \\ + 4\cdot 10^{19}\cdot\exp\left[-\frac{(z - 55)^2}{140}\right] \tag{A.8}$$

$$n_o(z) = 6\cdot 10^{22}\cdot\exp\left[-\frac{z}{4.5}\right] + 1.2\cdot 10^{21} - 6\cdot 10^{22}\cdot\frac{200}{z^2 + 100^2} \tag{A.9}$$

Condition 4

$$T_e(z) = 2.1\cdot 10^4\cdot\exp\left[-\frac{z}{450}\right] - 4.1\cdot 10^4\cdot\frac{20}{z^2 + 10^2} \tag{A.10}$$

$$n_e(z) = 3\cdot 10^{21}\cdot\exp\left[-\frac{z}{3}\right] + 9\cdot 10^{17}\cdot(590 - z) \tag{A.11}$$

$$n_o(z) = 3\cdot 10^{22}\cdot\exp\left[-\frac{z}{3}\right] + 3\cdot 10^{20} - 1.4\cdot 10^{21}\cdot\frac{26}{(z - 40)^2 + 13^2} - \\ - 2\cdot 10^{17}\cdot z \tag{A.12}$$

Appendix B

The energy balance for the electrons reads for a stationary plasma [28]

$$\nabla\cdot\left[\frac{3}{2}n_e k_b T_e \mathbf{w}_e\right] + n_e k_b T_e \nabla\cdot\mathbf{w}_e + \boldsymbol{\Pi}_e:\nabla\mathbf{w}_e + \nabla\cdot\mathbf{q}_e = Q^e \qquad (A.13)$$

where $\boldsymbol{\Pi}_e:\nabla\mathbf{w}_e$ represents the viscous dissipation, $\nabla\cdot\mathbf{q}_e$ the heat conduction and Q^e all other energy supplied to the electrons by collisions with other particles.
In this appendix expressions are given for the heat conduction, viscous dissipation and all the source terms occurring in the electron energy balance (equation A.13).

Heat conduction

The thermal heat flux $\mathbf{q}_e$ is [28]

$$\mathbf{q}_e = -\frac{1.82\cdot 10^{-10}}{\ln\Lambda_c} T_e^{5/2}\nabla T_e \qquad (A.14)$$

From this the heat conduction is

$$\nabla\cdot\mathbf{q}_e = -\frac{1.82\cdot 10^{-10}}{\ln\Lambda_c}\left[T_e^{5/2}\nabla^2 T_e + \frac{5}{2}T_e^{3/2}(\nabla T_e)^2\right] \qquad (A.15)$$

On the plasma axis this becomes:

$$\nabla\cdot\mathbf{q}_e = -\frac{1.82\cdot 10^{-10}}{\ln\Lambda_c}\left[T_e^{5/2}\frac{\partial^2 T_e}{\partial z^2} + \frac{5}{2}T_e^{3/2}\left[\frac{\partial T_e}{\partial z}\right]^2\right] \qquad (A.16)$$

Viscous dissipation

The viscous dissipation becomes on the plasma axis [28]

$$\boldsymbol{\Pi}_e:\nabla\mathbf{w}_e = -\frac{3.72\cdot 10^{-18} T_e^{5/2}}{n_e^2 \ln\Lambda_c} w_{ez}^2\left[\frac{\partial n_e}{\partial z}\right]^2 \qquad (A.17)$$

Source terms

$$Q^e = Q_{eh}{}^e + Q_{3d}{}^e + Q_{fb}{}^e + Q_{ff}{}^e + Q_{ohm}{}^e \tag{A.18}$$

where:

$Q_{eh}{}^e$ represents the elastic energy exchange with the ions and the neutrals;
$Q_{3d}{}^e$ is the energy loss due to collisional excitation/deexcitation and ionization/three–particle recombination (energy loss term);
$Q_{fb}{}^e$ represents the radiative recombination (energy loss term);
$Q_{ff}{}^e$ represents the brehmstrahlung (energy loss term);
$Q_{ohm}{}^e$ represents the Ohmic heating of the electrons (energy gain term).

a Elastic collisions with ions and neutrals

$$Q_{ei}{}^e = -3 \cdot \frac{m_e}{m_i} n_e \frac{1}{\tau_{ei}} k_b (T_e - T_i)$$

$$= -2.07 \cdot 10^{-33} \ln\Lambda_c \frac{n_e{}^2}{T_e{}^{3/2}} (T_e - T_i) \tag{A.19}$$

$$Q_{ea}{}^e = -3 \cdot \frac{m_e}{m_o} n_e \frac{1}{\tau_{eo}} k_b (T_e - T_o)$$

$$= -9.99 \cdot 10^{-43} n_e n_o T_e{}^{3/10} (T_e - T_o) \tag{A.20}$$

where $\ln\Lambda_c$ is the Coulomb logarithm, τ_{ei} and τ_{eo} are the relaxation times for momentum transfer between electrons and ions respectively electrons and neutrals; τ_{ei} is given by equation 5.17 and τ_{eo} is [22]

$$\tau_{eo} = \frac{5.7 \cdot 10^{14}}{n_o T_e{}^{3/10}} \tag{A.21}$$

b Inelastic processes

$$Q_{3d}{}^e = -n_e n_{1s} K_{1*} \delta b_1 E_{1*}$$

$$= -2.60 \cdot 10^{-51} \frac{n_e{}^3}{T_e{}^2} \delta b_1 \tag{A.22}$$

where K_{1+} is the collision coefficient, $E_{1+} = 2.524 \cdot 10^{-18}$ J the excitation energy of the ground state and $\delta b_1 = n_1/n_{1s} - 1$ the overpopulation of the ground state.

$$Q_{fb}{}^e = -n_+ A_{+1} \tfrac{3}{2} k_b T_e$$

$$= -3.08 \cdot 10^{-41}\, n_e{}^2 T_e{}^{1/2} \qquad \text{(A.23)}$$

where $n_+ = n_e$ and $A_{+1} = n_e K_{+1}{}^{(2)}$ the radiative transition probability with $K_{+1}{}^{(2)}$ the radiative collision coefficient.

$$Q_{ff}{}^e = -1.80 \cdot 10^{-40} n_e{}^2 T_e{}^{1/2} \qquad \text{(A.24)}$$

$$Q_{ohm}{}^e = \eta \mathbf{j} \cdot \mathbf{j} = 3.31 \cdot 10^{-36} \ln\Lambda_c \frac{n_e{}^2}{T_e{}^{3/2}} (\mathbf{w}_e - \mathbf{w}_i)^2 \qquad \text{(A.25)}$$

where $\eta = \dfrac{m_e}{n_e e^2 \tau_{ei}}$ is the resistivity of the plasma.